Thermal fluctuations and vortex lattice structures in chiral *p*-wave superconductors: Robustness of double-quanta vortices

Fredrik Nicolai Krohg [1,2] Egor Babaev,[3] Julien Garaud,[4] Håvard Homleid Haugen [1,2] and Asle Sudbø [1,2]

[1]*Department of Physics, Norwegian University of Science and Technology, NO-7491 Trondheim, Norway*
[2]*Center for Quantum Spintronics, Department of Physics, Norwegian University of Science and Technology, NO-7491 Trondheim, Norway*
[3]*Department of Physics, KTH-Royal Institute of Technology, Stockholm SE-10691, Sweden*
[4]*Institut Denis Poisson CNRS-UMR 7013, Université de Tours, 37200 Tours, France*

We use large-scale Monte-Carlo simulations to study thermal fluctuations in chiral *p*-wave superconductors in an applied magnetic field in three dimensions. We consider the thermal stability of previously predicted unusual double-quanta flux-line lattice ground states in such superconductors. In previous works it was shown that, neglecting thermal fluctuations, a chiral *p*-wave superconductor forms a hexagonal lattice of doubly-quantized vortices, except extremely close to the vicinity of H_{c2} where double-quanta vortices split apart. We find dissociation of double-quanta vortices driven by thermal fluctuations. However, our calculations also show that the previous predictions of hexagonal doubly-quantized vortices, where thermal fluctuations were ignored, are very robust in the considered model.

I. INTRODUCTION

Higher angular momentum odd-parity chiral superfluid and superconducting states are highly nontrivial pairing symmetries that result in novel topological as well as thermodynamic properties. Examples are chiral *p*-wave and chiral *f*-wave states. A prominent example of a condensed matter system where such a phase is firmly established is within the very rich phase diagram of superfluid ^{3}He, where the so-called *A* phase is a chiral *p*-wave superfluid. This unconventional superfluid phase was first discovered in seminal works of Osheroff *et al.* [1–4]. It is the interplay between spin and orbital degrees of freedom, with the multicomponent nature of the matter field of the superfluid or superconducting states, that makes the physics of such condensates much richer than the corresponding physics in simple superfluids like ^{4}He [5]. The *A* phase of ^{3}He has been used to explain exotic phenomena such as a nonvanishing orbital angular momentum in thermal equilibrium and unconventional dissipation behavior due to coreless vortex textures [6–8].

On the other hand, chiral *p*-wave pairing in solid state systems, i.e., superconductors, has remained less well established. One candidate superconductor with such chiral pairing that has been intensely investigated since its discovery is the superconducting phase of Sr_2RuO_4 [9]. The crystallographic structure of this compound is a perovskite, similar to the high T_c cuprates. The normal metallic phase features transport properties consistent with a 2D strongly correlated Fermi liquid phase [10], and superconductivity arises out of this normal state at $T \approx 1.5$ K. Contrary to the high-T_c cuprates however, Sr_2RuO_4 is a weak-coupling superconductor. For an early review of the basics physics and superconductivity of Sr_2RuO_4, see Ref. [11].

Conventional pairing is excluded in Sr_2RuO_4 by the many unusual experimental properties of Sr_2RuO_4. Early works revealed a number of unusual features and gave indication of chiral *p*-wave superconductivity. The early experimental results included the indication of suppression of superconductivity by nonmagnetic impurities [12–14]. A conventional superconductor is expected to have a T_c independent of addition of small fractions of such impurities but rather depend only on the number of magnetic impurities. Early NMR Knight shift experiments showed a temperature-independent Knight shift and thus a residual spin susceptibility as $T \rightarrow 0$, which is a hallmark of spin-triplet pairing [15,16]. Instead of being isotropic, the gap in Sr_2RuO_4 is indicated to contain line nodes or near nodes by both the temperature dependence of the specific heat and thermal conductivity as well as scanning tunneling microscopy measurements of the density of states. Other early works on the anisotropy of the thermal conductivity also were interpreted in favor of chiral *p*-wave pairing state [17–19]. Evidence for unconventional pairing in Sr_2RuO_4 is provided by the combination of evidence for spontaneous breaking of time-reversal symmetry and spin-triplet pairing. Muon spin-relaxation experiments find spontaneous magnetization in the superconducting state. Kerr effect experiments find a temperature dependent Kerr twisting angle [20–22] which, significantly, depends on the sign of the magnetic field.

One of the main predictions of theories of superconductors with chiral *p*-wave symmetry is the existence of domains of different chiralities of the superconducting order parameter, and as a result of this, the existence of chiral edge currents between domains of different chirality. These chiral edge currents should produce magnetic signatures observable by scanning Hall probe microscopy. No experimental proof of such chiral edge currents exists, in spite of several attempts to detect them [23]. Another issue is that recent ^{17}O Knight shift results have seen a substantial reduction of spin susceptibility at low temperatures, which led to recently

strengthened arguments against the hypothesis of spin-triplet pairing [24]. However, the evidence for spontaneous symmetry breaking [21,22], ultrasound [25], thermodynamics [26], and unconventional vortex physics [27] strongly indicates a multicomponent order parameter. Recent works suggested the possibility of chiral d-wave, $s + id$, and $s + ig$ order parameters for the superconducting state of Sr_2RuO_4 [26,28,29]. The intense experimental pursuit and controversies associated with chiral p-wave pairing motivates the current work focused on magnetic response of such systems. Moreover, the model we consider is consistent with a certain chiral d-wave order parameter [28] that is presently discussed in connection with Sr_2RuO_4.

Furthermore, UPt_3 is a heavy fermion topological type-II superconductor with an unconventional superconducting state believed to be a chiral f-wave pairing state with E_{2u} irreducible representation. At a phenomenological level, it can be described by a Ginzburg-Landau (GL) theory of a two-component complex matter field with the components related by a time-reversal transformation and oppositely directed internal orbital angular momentum [30]. The experimental evidence for such a two-component description of the superconducting state of UPt_3 was recently strengthened when its time-reversal symmetry breaking character was demonstrated by showing that the energy of the vortex lattice state depends on the relative direction of the external magnetic field [31]. The theoretical description we will use is thus relevant to this system.

Early numerical work showed that such a two-component GL theory for UPt_3 admits anisotropic vortices with nontrivial core structures and a hexagonal vortex lattice consisting of doubly-quantized vortices at field strengths $H < 0.3H_{c2}$ in the ground state [32]. At higher field strengths $H > 0.3H_{c2}$, the doubly-quantized vortices were found to dissociate into singly-quantized vortices. However, the lattice symmetry of the resulting singly-quantized aggregate vortex state was not determined.

The GL theory used in this paper, which posits a chiral symmetry of the superconducting state, is based on the (two-dimensional) Γ_{5u}^- representation of the D_{4h} symmetry group [33]. Lowest Landau-level calculations based on this GL theory have predicted a square lattice of vortices when the external magnetic field is applied parallel to the c axis for high field strengths close to upper critical H_{c2} [34]. For fields parallel to the c axis close to the lower critical field H_{c1}, an extended London theory predicted a singly-quantized rectangular vortex lattices continuously deforming to singly-quantized square vortex lattices as the magnetic field strength was increased [35]. (Below we will define precisely what is meant by singly-quantized and doubly-quantized vortices.) Numerical energy minimization of the free energy has shown that isolated doubly-quantized vortices are generically stable and actually are energetically favorable compared to two isolated single-quanta vortices [36,37]. In a part of parameter space, this is corroborated by calculations of isolated topological defects based on Eilenberger's equation where a Γ_{5u}^- symmetry was assumed [38]. This led to the expectation that double-quanta vortices form hexagonal lattices, while the single-quanta vortices form square lattices based on the symmetry of the current distribution of the isolated vortices.

The numerical studies of isolated vortices were extended to a finite ensemble of vortices in Ref. [39], where a finite-element method was used to minimize the GL free energy when increasing the external magnetic field strength. These computations found a robust hexagonal lattice of doubly-quantized vortices at field strengths up to a very close vicinity of H_{c2} when the field was parallel to the c axis. This is inconsistent with the vortex phase diagram of Sr_2RuO_4 [27]. To examine the vortex structure at fields close to H_{c2}, a temperature dependence was inserted into the quadratic coefficient of the free energy which allowed the system to be moved horizontally in the T-H phase space. Extremely close to H_{c2}, the double-quanta vortices were seen to dissociate into single-quanta vortices that arranged themselves in a square lattice through a mixed phase where both single and double quanta vortices were present. This type of behavior was, on one hand, quite robust, but on the other hand has never been observed in the materials that are candidates for chiral superconductivity.

The manner in which thermal effects were included in Ref. [39] was at a mean field level, i.e., entropic effects were not fully accounted for. This then leaves open the question of whether these unusual vortex states and the field-induced transitions between them are actually stable when thermal fluctuations are included. In particular, a weak binding energy as well as different entropic contributions of different lattices can alter the conclusion of the dominant character of two-quanta vortex lattice.

In other words, we will investigate in this paper whether the predicted field regime of a transition from a doubly-quantized hexagonal to a square singly-quantized vortex lattice with increasing temperature [39] is dramatically over- or under-estimated by not fully accounting for entropic effects. This is particularly important in this system because the mean-field-based Ginzburg-Landau model in an external field gives two different vortex-lattice states that are close in free energy. Moreover, the mean-field results found the transition from one vortex lattice to the other at a temperature of about 80% of the zero-field critical temperature T_c. At such elevated temperatures it is by no means obvious that thermal entropic effects can be neglected, even though the thermal fluctuations are not critical. Thus, an assessment of whether the conclusion based on a mean-field analysis is robust against more accurate estimates of the entropy of the system is required. Specifically, we attempt to answer if the double-quanta vortex lattice survives inclusion of thermal fluctuations since there is more entropy in a single-quanta vortex lattice, opening the possibility that it may be entropically stabilized at substantially lower fractions of T_c than the mean-field calculation would predict. Our approach is related in spirit to that of Ref. [40], where a decay of single-quanta vortex lattice into a half-quanta lattice was considered at elevated temperatures.

The purpose of the present paper is therefore to consider the stability of doubly-quantized hexagonal vortex lattices and singly-quantized square vortex lattices when all thermal fluctuation effects are included in gauge fields and phases of the complex matter fields. In strongly type-II one-component superconductors, a good approximation is to neglect amplitude fluctuations [41–46]. In chiral superconductors, the situation is more subtle because of a number of massive normal modes that are linear combinations of phase modes, magnetic modes,

and amplitude modes [47]. Then the London-like approximation amounts to dropping the most massive modes and neglecting some of the mixing.

We present the results of extensive Monte-Carlo simulations of a chiral p-wave GL theory with an external field parallel to the c axis. This paper is organized as follows. In Sec. II, we present in detail the model we will consider, along with a discussion of its parametrization. We then discuss a subtle point on the discretization of this model on a numerical grid and the choice of basis for the two-component matter field. In Sec. III, we present details of the Monte-Carlo simulations along with definitions of the observables we will use. In Sec. IV, we present results of our detailed Monte-Carlo simulations at a filling fraction f of field-induced vortices of $f = 1/64$ at various temperatures, starting from high temperatures and proceeding to lower temperatures. We find two types of stable vortex lattices and an interesting transition region where the vortex lattices thermally reconstruct. Conclusions are presented in Sec. VI. Some mathematical details are relegated to appendices.

II. GINZBURG-LANDAU MODEL

A. Dimensionless units and reduction of parameters

We consider the clean limit of the Ginzburg-Landau energy density of the two-dimensional Γ_{5u} irreducible representation of the tetragonal D_{4h} symmetry group which in the chiral basis using dimensionless variables and units reads [35,39]

$$\mathcal{F} = g^{-2}|\nabla \times \mathbf{A}|^2 + |D_x \boldsymbol{\eta}|^2 + |D_y \boldsymbol{\eta}|^2 + 2\tilde{\kappa}_5 |D_z \boldsymbol{\eta}|^2 \quad (1\text{a})$$

$$+ (1 + \nu)\,\mathrm{Re}[(D_x \eta_+)^* D_x \eta_- - (D_y \eta_+)^* D_y \eta_-] \quad (1\text{b})$$

$$- (1 - \nu)\,\mathrm{Im}[(D_x \eta_+)^* D_y \eta_- + (D_y \eta_+)^* D_x \eta_-] \quad (1\text{c})$$

$$+ 2|\eta_+ \eta_-|^2 + \nu\,\mathrm{Re}(\eta_+^{*2}\eta_-^2) + \sum_{h=\pm}\left(-|\eta_h|^2 + \frac{1}{2}|\eta_h|^4\right). \quad (1\text{d})$$

The two dimensions of the representation are spanned by the complex fields $\eta_\pm$. The covariant derivative $D_a = \nabla_a - iA_a$, and ν and g are dimensionless material parameters with the restriction that $|\nu| < 1$. Deriving the effective Ginzburg-Landau energy from a microscopic model [48], it is seen that $\nu = (\langle v_x^4 \rangle - 3\langle v_x^2 v_y^2\rangle)/(\langle v_x^4 \rangle + \langle v_x^2 v_y^2\rangle)$, where v_a is the a component of the Fermi velocity and the brackets: $\langle \cdot \rangle$ indicate an average over the Fermi surface. ν thus parameterizes the anisotropy of the Fermi surface in that $\nu = 0$ for a cylindrical surface, while $\nu \neq 0$ for a Fermi surface distorted by fourfold anisotropy.

The model in Eq. (1) is a restricted version of the full Γ_{5u} free energy which in SI units can be written [33,35,49]

$$\mathcal{F} = -\alpha|\boldsymbol{\eta}|^2 + \frac{\beta_1}{2}|\boldsymbol{\eta}|^4 + \frac{\beta_2}{2}(\eta_x \eta_y^* - \eta_y \eta_x^*)^2 + \beta_3|\eta_x \eta_y|^2$$
$$+ \kappa_1(|D_x \eta_x|^2 + |D_y \eta_y|^2) + \kappa_2(|D_y \eta_x|^2 + |D_x \eta_y|^2)$$
$$+ \kappa_3[(D_x \eta_x)^* D_y \eta_y + (D_y \eta_y)^* D_x \eta_x]$$
$$+ \kappa_4[(D_x \eta_y)^* D_y \eta_x + (D_y \eta_x)^* D_x \eta_y]$$
$$+ \kappa_5(|D_z \eta_x|^2 + |D_z \eta_y|^2) + \frac{|\nabla \times \mathbf{A}|^2}{2\mu_0}, \quad (2)$$

TABLE I. Name, mean-field energy density, and solution modulo an overall phase of the mean field minimization of $\mathcal{F}$ in Eq. (4). The A phase is the phase that exhibits spontaneous time-reversal symmetry breaking in zero magnetic field and is the one we focus on in this paper. The B and C phases are time-reversal symmetric odd-parity superconducting states with line nodes in the gap on the Fermi surface.

Name	$\mathcal{F}$	(η_+, η_-)	u^2
A phase	$-\dfrac{\alpha^2}{2(\beta_1 - \beta_2) + \beta_3}$	$u(0, 1) \vee u(1, 0)$	$\dfrac{2\alpha}{2(\beta_1 - \beta_2) + \beta_3}$
B phase	$-\dfrac{\alpha^2}{2\beta_1 + \beta_3}$	$u(\pm i, 1)$	$\dfrac{\alpha}{2\beta_1 + \beta_3}$
C phase	$-\dfrac{\alpha^2}{2\beta_1}$	$u(\pm 1, 1)$	$\dfrac{\alpha}{2\beta_1}$

where $D_a = \nabla_a - i(q/\hbar)A_a$, q is the charge of the Cooper pair, $\hbar$ is Planck's reduced constant, and μ_0 is the vacuum permeability. In this expression, the conventional xy basis is used for the complex fields η_x and η_y. Rotating this to the chiral basis through the transformation

$$\eta_\pm = \frac{1}{\sqrt{2}}(\eta_x \pm i\eta_y) \quad (3)$$

yields the energy density

$$\mathcal{F} = -\alpha|\boldsymbol{\eta}|^2 + (2(\beta_1 - \beta_2) + \beta_3)\frac{|\eta_+|^4 + |\eta_-|^4}{4}$$
$$+ (\beta_1 + \beta_2)|\eta_+ \eta_-|^2 - \frac{\beta_3}{2}\,\mathrm{Re}\,\eta_+^2 \eta_-^{*2}$$
$$+ \frac{\kappa_1 + \kappa_2}{2}(|D_x \boldsymbol{\eta}|^2 + |D_y \boldsymbol{\eta}|^2) + \kappa_5|D_z \boldsymbol{\eta}|^2$$
$$+ (\kappa_1 - \kappa_2)\,\mathrm{Re}[D_x \eta_+ (D_x \eta_-)^* - D_y \eta_+ (D_y \eta_-)^*]$$
$$+ (\kappa_4 - \kappa_3)\,\mathrm{Im}[D_x \eta_+ (D_y \eta_+)^* + D_y \eta_- (D_x \eta_-)^*]$$
$$+ (\kappa_4 + \kappa_3)\,\mathrm{Im}[D_x \eta_+ (D_y \eta_-)^* + D_y \eta_+ (D_x \eta_-)^*]$$
$$+ \frac{|\nabla \times \mathbf{A}|^2}{2\mu_0}. \quad (4)$$

Taking the mean field limit and looking at the fourth-order terms yields the constraint that for the mean field energy to be bounded from below, $\beta_1 > 0$, $\beta_3 > -2\beta_1$, and $\beta_3 > 2(\beta_2 - \beta_1)$. Minimizing $\mathcal{F}$ w.r.t. $\eta_\pm$ yields the three distinct mean field solutions in Table I. The regions of the β_3/β_1, β_2/β_1-parameter space for which each of these solutions minimizes $\mathcal{F}$ is shown in Fig. 1. One of these solutions, known as the A phase, exhibits spontaneous time-reversal symmetry breaking. This is the phase we are interested in examining.

We now focus on the A phase. To write $\mathcal{F}$ on a dimensionless form, we scale the dimensionless energy density $\tilde{\mathcal{F}}$ and dimensionless fields $\tilde{\eta}_\pm$ by their mean field values in the A phase such that $\mathcal{F} = 2\alpha^2/[2(\beta_1 - \beta_2) + \beta_3]\tilde{\mathcal{F}}$ and $\eta_\pm = \sqrt{2\alpha/[2(\beta_1 - \beta_2) + \beta_3]}\tilde{\eta}_\pm$. We also choose the length scale such that the coefficient in front of the first term in the kinetic part of $\mathcal{F}$ becomes trivial in dimensionless units, i.e., $\nabla_a = \sqrt{2\alpha/(\kappa_1 + \kappa_2)}\tilde{\nabla}_a$. Finally we scale the gauge field $A_a = \hbar\sqrt{2\alpha/(\kappa_1 + \kappa_2)}/q\tilde{A}_a$ such that $\tilde{D}_a = \tilde{\nabla}_a - i\tilde{A}_a$. To simplify the notation, we neglect the tilde in the dimensionless variables in the following. With these choices of units, $\mathcal{F}$ takes
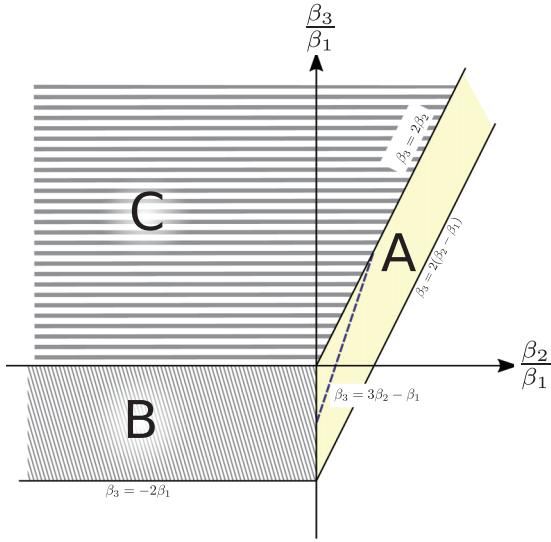
FIG. 1. Mean field phase diagram spanned by the fourth order material constants β_i. The A, B, and C regions correspond to the mean field solutions given in Table I. The white region below the phases give unbounded mean field energy and is unphysical. The blue line $\beta_3 = 3\beta_2 - \beta_1$ gives the values of parameter space spanned by the parameter choices used in the reduced free energy density. This line can be parametrized in terms of the single dimensionless parameter ν for $-1 < \nu < 1$.

the dimensionless form

$$
\mathcal{F} = -|\boldsymbol{\eta}|^2 + \frac{|\eta_+|^4 + |\eta_-|^4}{2} + \frac{2}{1 + \Delta\tilde{\beta}}|\eta_+\eta_-|^2 + \nu\,\mathrm{Re}\,\eta_+^2\eta_-^{*2}
$$
$$
+ |D_x\boldsymbol{\eta}|^2 + |D_y\boldsymbol{\eta}|^2 + 2\tilde{\kappa}_5|D_z\boldsymbol{\eta}|^2 + \frac{|\nabla \times \mathbf{A}|^2}{g^2}
$$
$$
+ (1 + \nu_k)\,\mathrm{Re}[D_x\eta_+(D_x\eta_-)^* - D_y\eta_+(D_y\eta_-)^*]
$$
$$
+ \Delta\tilde{k}\,\mathrm{Im}[D_x\eta_+(D_y\eta_+)^* + D_y\eta_-(D_x\eta_-)^*]
$$
$$
+ (\nu_k - 1 - 2\Delta)\,\mathrm{Im}[D_x\eta_-(D_y\eta_+)^* + D_y\eta_-(D_x\eta_+)^*],
$$
$$
\tag{5}
$$

for dimensionless parameters

$$
\Delta\tilde{\beta} = \frac{\beta_3 - 3\beta_2 + \beta_1}{\beta_1 + \beta_2}, \tag{6a}
$$

$$
\nu = \frac{\beta_3}{2(\beta_2 - \beta_1) - \beta_3}, \tag{6b}
$$

$$
\nu_k = \frac{\kappa_1 - 3\kappa_2}{\kappa_1 + \kappa_2}, \tag{6c}
$$

$$
\Delta\tilde{k} = 2\frac{\kappa_4 - \kappa_3}{\kappa_1 + \kappa_2}, \tag{6d}
$$

$$
\Delta = \frac{\kappa_3 + \kappa_4 - 2\kappa_2}{\kappa_1 + \kappa_2}, \tag{6e}
$$

$$
\tilde{\kappa}_5 = \frac{\kappa_5}{\kappa_1 + \kappa_2}, \tag{6f}
$$

$$
g = \frac{q}{\hbar}\sqrt{\mu_0 \frac{(\kappa_1 + \kappa_2)^2}{2(\beta_1 - \beta_2) + \beta_3}}. \tag{6g}
$$

So far, no assumptions have been made about the values of the material parameters α, β_i, and κ_i. Based on microscopic derivations of the kinetic constants in the weak coupling and clean limit [48], we have that $\kappa_2 = \kappa_3 = \kappa_4 \propto \langle v_x^2 v_y^2 \rangle$ and $\kappa_1 \propto \langle v_x^4 \rangle$. For the case of a cylindrical Fermi surface, another microscopic derivation of the Ginzburg-Landau coefficients [50] shows that in the weak coupling approximation the relations $\beta_2/\beta_1 = \kappa_2/\kappa_1$ and $\beta_3 = 3\beta_2 - \beta_1$ hold. The validity of these constraints has been extended to noncylindrical Fermi surfaces in Refs. [34,49]. Using these relationships, we see that $\Delta\tilde{\beta} = \Delta\tilde{k} = \Delta = 0$, $g = q/\sqrt{\mu_0\kappa_1^2(1 + \kappa_2/\kappa_1)/\beta_1}/\hbar$, and $\nu = \nu_k$, such that Eq. (5) reduces to Eq. (1) with the previously mentioned interpretation of ν as measuring the Fermi surface anisotropy.

The weak coupling relationship $\beta_3 = 3\beta_2 - \beta_1$ constrains the system to be along the blue dashed line in parameter space in Fig. 1. This line can in turn be parametrized in terms of ν such that $\beta_2/\beta_1 = (1 - \nu)/(\nu + 3)$ and $\beta_3/\beta_1 = -4\nu/(\nu + 3)$. From the discussion in the last paragraph, we can show that ν can be expressed in terms of Fermi-surface averages over Fermi velocities as described below Eq. (1). From this interpretation it follows that a cylindrical, i.e., isotropic Fermi surface is equivalent with $\nu = 0$, while a square, i.e., anisotropic Fermi surface is equivalent with $\nu = \pm 1$. Going back to the interpretation of ν as given in terms of the β parameters, we thus see that the Fermi surface is cylindrically symmetric for $3\beta_2 = \beta_1$, which is where the blue line crosses the x axis in Fig. 1. As ν approaches 1, where the Fermi surface must be square, the system approaches the B phase. As ν approaches -1, the system approaches the C phase instead.

B. Lattice Ginzburg Landau model

The GL energy $E = \int \mathcal{F}\,d^3r$ in Eq. (1) is discretized on a 3D cubic lattice of points $\mathbf{r}$ containing values for the complex fields $\eta_{\mathbf{r}}^\pm$ as well as link variables

$$
A_{\mathbf{r},\mu} = \int_{\mathbf{r}}^{\mathbf{r}+l\hat{\mu}} A_\mu(\mathbf{r})\,dr_\mu \tag{7}
$$

between the points at $\mathbf{r}$ and $\mathbf{r} + l\hat{\mu}$, where l is the lattice point separation spacing. On the lattice, $E = \int \mathcal{F}\,d^3r$ is written as a lattice sum over the discretized energy density

$$
E = l^3 \sum_{\mathbf{r}} \mathcal{F}^{\mathbf{r}}, \tag{8}
$$

where $\mathbf{r}$ runs over the sites of the numerical lattice and the lattice energy density $\mathcal{F}^{\mathbf{r}}$ is given by

$$
\mathcal{F}^{\mathbf{r}} = \mathcal{F}_{\mathrm{K}}^{\mathbf{r}} + \mathcal{F}_{\mathrm{An}}^{\mathbf{r}} + \mathcal{F}_{\mathrm{MG}}^{\mathbf{r}} + \mathcal{F}_{\mathrm{V}}^{\mathbf{r}} + \mathcal{F}_{\mathrm{A}}^{\mathbf{r}}. \tag{9}
$$

This defines an effective lattice gauge theory derived from the continuum theory in Eq. (1). In Eq. (9), $\mathcal{F}^{\mathbf{r}}$ is split into various gradient terms, a potential-energy term $\mathcal{F}_{\mathrm{V}}^{\mathbf{r}}$, and a magnetic field energy density term $\mathcal{F}_{\mathrm{A}}^{\mathbf{r}}$, respectively. The gradient terms have been written as a sum of three different terms to be detailed below, namely a standard isotropic term $\mathcal{F}_{\mathrm{K}}^{\mathbf{r}}$, a term contributing to anisotropy in the kinetic energy $\mathcal{F}_{\mathrm{An}}^{\mathbf{r}}$, and a mixed gradient term $\mathcal{F}_{\mathrm{MG}}^{\mathbf{r}}$.

In the discretized energy density, covariant derivatives are treated by a forward difference scheme

$$D_\mu \eta^h = (\partial_\mu - iA_\mu)\eta^h \mapsto l^{-1}\big(\eta^h_{\mathbf{r}+l\hat{\mu}}e^{-ilA_{\mathbf{r},\mu}} - \eta^h_\mathbf{r}\big), \quad (10)$$

where the field value $\eta^h_{\mathbf{r}+l\hat{\mu}}$ has been parallel transported back to the point $\mathbf{r}$ via the Abelian U(1) parallel transporter $U_{\mathbf{r},\mu} = e^{-ilA_{\mathbf{r},\mu}}$ [51]. In the following, we set the lattice spacing $l = 1$.

Writing the complex fields $\eta^h_\mathbf{r}$ in terms of their amplitudes $\rho^h_\mathbf{r}$ and phases $\theta^h_\mathbf{r}$, the discretized expression derived from the kinetic part of $\mathcal{F}$ given by the covariant derivatives in Eq. (1a) is written on the standard cosine form [52]

$$\mathcal{F}^{\mathbf{r}}_K = 2\sum_{\mu,h}\big[\rho^{h\,2}_\mathbf{r} - \rho^h_\mathbf{r}\rho^h_{\mathbf{r}+\hat{\mu}}\cos\big(\theta^h_{\mathbf{r}+\hat{\mu}} - \theta^h_\mathbf{r} - A_{\mathbf{r},\mu}\big)\big]. \quad (11)$$

Here, h denotes the two chiral components $h \in \{\pm\}$, while $\mu \in \{x, y, z\}$ and we have set the parameter $\tilde{\kappa}_5 = 1/2$ such as to make the kinetic energy density isotropic.

Introducing the notation $\bar{h} = -h$, $q \in \{x, y\}$ and the symbol $\zeta_{\alpha\beta} = 1 - 2\delta_{\alpha\beta}$, the anisotropic part of $\mathcal{F}$ in Eq. (1b) is discretized to

$$\mathcal{F}^{\mathbf{r}}_{An} = (1 + \nu)\sum_{qh}\zeta_{qy}\rho^{\bar{h}}_\mathbf{r}\rho^h_{\mathbf{r}+\hat{q}}\cos\big(\theta^h_{\mathbf{r}+\hat{q}} - \theta^{\bar{h}}_\mathbf{r} - A_{\mathbf{r},q}\big). \quad (12)$$

These terms mix the two components and give different signs of the contributions depending on the direction $\hat{q}$, i.e., anisotropic contributions to the kinetic energy.

The contribution $\mathcal{F}^{\mathbf{r}}_{MG}$ in Eq. (9) is named the mixed gradient terms since these terms mix the gradient directions as well as the different components as seen in Eq. (1c). In the discretized form, it is given by

$$\begin{aligned}
\mathcal{F}^{\mathbf{r}}_{MG} = -&(1 - \nu)\sum_q\Bigg[\rho^+_\mathbf{r}\rho^-_\mathbf{r}\sin(\theta^-_\mathbf{r} - \theta^+_\mathbf{r}) \\
&+ \sum_h\zeta_{+h}\rho^h_{\mathbf{r}+\hat{q}}\rho^{\bar{h}}_\mathbf{r}\sin\big(\theta^h_{\mathbf{r}+\hat{q}} - \theta^{\bar{h}}_\mathbf{r} - A_{\mathbf{r},q}\big) \\
&+ \rho^+_{\mathbf{r}+\hat{q}}\rho^-_{\mathbf{r}+\hat{q}}\sin(\theta^-_{\mathbf{r}+\hat{q}} - \theta^+_{\mathbf{r}+\hat{q}} - (A_{\mathbf{r},q} - A_{\mathbf{r},\bar{q}}))\Bigg],
\end{aligned} \quad (13)$$

where $\bar{q} \in \{x, y\} \setminus \{q\}$.

The discretized potential part of $\mathcal{F}^{\mathbf{r}}$ is written as

$$\begin{aligned}
\mathcal{F}^{\mathbf{r}}_V = &(\rho^+_\mathbf{r}\rho^-_\mathbf{r})^2(2 + \nu\cos 2(\theta^+_\mathbf{r} - \theta^-_\mathbf{r})) \\
&+ \sum_h\Big[-(\rho^h_\mathbf{r})^2 + \frac{1}{2}(\rho^h_\mathbf{r})^4\Big].
\end{aligned} \quad (14)$$

The first term in Eq. (14) originates with the term $2|\eta_+\eta_-|^2 + \nu\,\mathrm{Re}(\eta_+^{*2}\eta_-^2)$ in Eq. (1d). Of particular interest in the present context is the factor $\cos 2(\theta^+_\mathbf{r} - \theta^-_\mathbf{r})$. This term is minimized for $2(\theta^+_\mathbf{r} - \theta^-_\mathbf{r}) = \pi$ for $\nu > 0$, thus potentially locking the phase difference, and breaking the global $U(1)$ invariance of the system associated with the phase difference $\theta^+_\mathbf{r} - \theta^-_\mathbf{r}$ down to $\mathbb{Z}_2$. The last line in Eq. (14) comes from the last term in Eq. (1d) and represents a soft constraint on the fluctuations of the amplitude $\rho^h_\mathbf{r}$. Finally, the gauge field energy is given a noncompact discretization [53] such that $A_{\mathbf{r},\mu} \in (-\infty, \infty)$ and

$$\mathcal{F}^{\mathbf{r}}_A = g^{-2}(\mathbf{\Delta} \times \mathbf{A}_\mathbf{r})^2 = g^{-2}\sum_{\mu>\lambda}(\Delta_\mu A_{\mathbf{r},\lambda} - \Delta_\nu A_{\mathbf{r},\lambda})^2, \quad (15)$$

where $\mu, \lambda \in \{x, y, z\}$ and $\Delta_\mu A_{\mathbf{r},\lambda} = A_{\mathbf{r}+\hat{\mu},\lambda} - A_{\mathbf{r},\lambda}$.

The model in Eq. (1) has thus been formulated on a lattice in terms of two parameters, namely the coupling constant of the gauge field to the matter field g and the parameter ν describing the anisotropy of the Fermi surface. We will consider the model in this restricted parameters space to make the problem tractable in Monte-Carlo simulations. The parameter values $\nu = 0.1$ and $g = 0.3$ have been used for most of the simulation results presented in this paper.

C. XY basis and pseudo-$\mathbb{CP}^1$ constraint

The full Ginzburg-Landau model is still too complex to simulate on a lattice of sufficient size. Therefore, a London approximation is typically used for this kind of problem (see, e.g., Refs. [41–46]). Taking the London limit in the chiral p-wave case, however, requires special care. As discussed in detail in Ref. [47], all phase and density degrees of freedom are in general coupled. However, as discussed in the same reference, the mixing between different modes for certain parameters is small, making the London limit an adequate approximation. The required conditions that must hold in this study are: (i) the dominant length scale in magnetic field should be much larger than the core size, and (ii) the external field should be sufficiently low so that vortex cores do not overlap. Since we are interested primarily in vortex dissociation transition, the binding energy comes from mixed gradient terms, which are retained in our approximation. The low temperature configuration we obtain is consistent with the solutions found at low temperatures in the full Ginzburg-Landau model [39].

To simplify the model, we introduce a pseudo-$\mathbb{CP}^1$ constraint on the complex fields $\eta^\pm$. Since these fields are related to corresponding xy-basis fields $\eta^a_\mathbf{r}$ for $a \in \{x, y\}$ through the orthonormal transformation in Eq. (3), we may rotate the expressions for the discretized free energy densities in Eqs. (14), (11), (12), and (13) back to this basis. It is this xy basis that is used in all simulations when evaluating the free energy for accepting new states through the Metropolis-Hastings algorithm, since, as we shall see, this ensures that mixed component terms are retained in the London limit.

The conventional kinetic energy contribution in Eq. (11) is invariant under the change of basis, such that

$$\mathcal{F}^{\mathbf{r}}_K = 2\sum_{a\mu}\big[\rho^{a\,2}_\mathbf{r} - \rho^a_{\mathbf{r}+\hat{\mu}}\rho^a_\mathbf{r}\cos\big(\theta^a_{\mathbf{r}+\hat{\mu}} - \theta^a_\mathbf{r} - A_{\mathbf{r},\mu}\big)\big]. \quad (16)$$

The expression for the onsite potential terms, however, becomes slightly more involved, perhaps most succinctly expressed as

$$\begin{aligned}
\mathcal{F}^{\mathbf{r}}_V = &(1 + \nu)\frac{\rho^{x\,4}_\mathbf{r} + \rho^{y\,4}_\mathbf{r}}{4} + \sum_a\Big[-\rho^{a\,2}_\mathbf{r} + \frac{1}{2}\rho^{a\,4}_\mathbf{r}\Big] \\
&+ (1 - \nu)(\rho^x_\mathbf{r}\rho^y_\mathbf{r})^2\Big[1 + \frac{1}{2}\cos 2(\theta^x_\mathbf{r} - \theta^y_\mathbf{r})\Big]. \quad (17)
\end{aligned}$$

The anisotropy term remains similar in both basis, with the xy-basis version having the form

$$\mathcal{F}^{\mathbf{r}}_{An} = (1 + \nu)\sum_{aq}\zeta_{aq}\rho^a_{\mathbf{r}+\hat{q}}\rho^a_\mathbf{r}\cos\big(\theta^a_{\mathbf{r}+\hat{q}} - \theta^a_\mathbf{r} - A_{\mathbf{r},q}\big), \quad (18)$$

the minor difference being that ζ_{aq} now depends on both summation indices. Finally, the mixed-gradient terms take the form

$$
\begin{aligned}
\mathcal{F}_{\mathrm{MG}}^{\mathrm{r}} = (1-\nu) \sum_a \Bigg[&\rho_{\mathbf{r}}^a \rho_{\mathbf{r}}^{\bar{a}} \cos\left(\theta_{\mathbf{r}}^a - \theta_{\mathbf{r}}^{\bar{a}}\right) \\
&- \sum_q \rho_{\mathbf{r}+\hat{q}}^a \rho_{\mathbf{r}}^{\bar{a}} \cos\left(\theta_{\mathbf{r}+\hat{q}}^a - \theta_{\mathbf{r}}^{\bar{a}} - A_{\mathbf{r},q}\right) \\
&+ \rho_{\mathbf{r}+\hat{x}}^a \rho_{\mathbf{r}+\hat{y}}^{\bar{a}} \cos\left(\theta_{\mathbf{r}+\hat{x}}^a - \theta_{\mathbf{r}+\hat{y}}^{\bar{a}} - (A_{\mathbf{r},x} - A_{\mathbf{r},y})\right) \Bigg]. \quad (19)
\end{aligned}
$$

The process of discretization commutes with the basis rotation, i.e., first rotating the basis in Eq. (1) and then discretizing the result yields the same expressions for $\mathcal{F}^{\mathrm{r}}$.

The model is now simplified by taking the London limit in the xy basis, i.e., neglecting xy-basis amplitude fluctuations such that $\rho_{\mathbf{r}}^a = \rho^a \forall \mathbf{r}$. The mean field A-phase solution of Eq. (1) in the xy basis gives amplitudes $\rho^x = \rho^y = 1/\sqrt{2}$ which will be used in the following. Using the xy basis has the comparative advantage over the chiral basis in that setting the London-limit amplitudes equal to the mean field solution amplitude values does not eliminate the mixed component terms. Taking the limit in the xy basis allows the chiral basis amplitudes to fluctuate since from Eq. (3) they are related to their xy counterparts through

$$
\rho_{\mathbf{r}}^{\pm 2} = \frac{\rho^{x\,2} + \rho^{y\,2}}{2} \pm \rho^x \rho^y \sin\left(\theta_{\mathbf{r}}^x - \theta_{\mathbf{r}}^y\right). \quad (20)
$$

From this equation, we see that the xy basis London limit implies the restriction

$$
\rho_{\mathbf{r}}^{+\,2} + \rho_{\mathbf{r}}^{-\,2} = \rho^{x\,2} + \rho^{y\,2} = 1, \quad (21)
$$

and in this sense the London limit in the xy basis may equivalently be viewed as a $\mathbb{CP}^1$ constraint on the chiral amplitudes $\rho_{\mathbf{r}}^h$. Note that a phase locking of $\theta_{\mathbf{r}}^x - \theta_{\mathbf{r}}^y = \pm\pi/2$ corresponds to spontaneous time-reversal symmetry breaking in zero magnetic field, i.e., $|\eta_{\mathbf{r}}^+|^2 \neq |\eta_{\mathbf{r}}^-|^2$.

Since the xy-basis London limit removes two real degrees of freedom from the problem, we expect two constraints in the chiral basis as well. The second constraint takes the form of the relationship

$$
\tan\theta_{\mathbf{r}}^+ = \tan\left(\theta_{\mathbf{r}}^- + \frac{\pi}{2}\right) \quad (22)
$$

between the chiral phases. A derivation of this relationship can be found in Appendix A. This implies that $\theta^+ = \theta^- + \pi/2 + \pi n$ for $n \in \{-2, -1, 0, 1\}$ since phases are defined compactly by $\theta \in [-\pi, \pi)$. That the phases are not completely locked to each other allows there to be a vortex singularity in one component independent of the other.

D. Symmetrization and lattice potential

The discretization procedure in Eq. (10) does not in general guarantee that the resulting discrete lattice free energy is symmetric under the same transformations as the original continuum theory. It only guarantees that the continuum limit of the discrete theory satisfies these symmetries. To ensure that the lattice energy density is invariant under a fourfold rotation of the numerical lattice, we introduce a symmetrization of the

discretized xy-basis free energy density as follows

$$
\mathcal{F}^{\mathrm{s}} = \tfrac{1}{4}\left[\mathcal{F}^{\mathrm{r}} + C_4 \mathcal{F}^{\mathrm{r}} + C_4^2 \mathcal{F}^{\mathrm{r}} + C_4^3 \mathcal{F}^{\mathrm{r}}\right], \quad (23)
$$

where C_4 is a counterclockwise rotation by $\pi/2$ radians about the $\hat{z}$ axis, and we allow lattice translations because of periodic boundary conditions (see next section).

Under this rotation, we let the gauge-field link variables $A_{\mathbf{r},\mu}$ transform as the components of a vector field such that

$$
C_4 : A_{\mathbf{r},\mu} = A_{C_4\mathbf{r}, C_4\mu}. \quad (24)
$$

Since link variables are only defined for positive directions from any numerical lattice point $\mathbf{r}$, we use the relationship $A_{\mathbf{r},-\mu} = -A_{\mathbf{r}-\hat{\mu},\mu}$ whenever the transformation in Eq. (24) results in a negative link direction. As a nontrivial example $C_4 : A_{\mathbf{r}+\hat{x},y} = -A_{C_4\mathbf{r}+\hat{y}-\hat{x},x}$.

To figure out how the complex fields η_a transform, we remember that they are the coefficients of the vector $\mathbf{d} = \sum_a \eta_a \mathbf{b}_a$ whose basis vectors $\{\mathbf{b}_a\}$ transform according to the irreducible representation Γ_{5u} [48]. Inserting the C_4 representation matrix then yields the transformation

$$
C_4 : \begin{pmatrix} \eta_{\mathbf{r}}^x \\ \eta_{\mathbf{r}}^y \end{pmatrix} = \begin{pmatrix} 0 & -1 \\ 1 & 0 \end{pmatrix} \begin{pmatrix} \eta_{C_4\mathbf{r}}^x \\ \eta_{C_4\mathbf{r}}^y \end{pmatrix} = \begin{pmatrix} -\eta_{C_4\mathbf{r}}^y \\ \eta_{C_4\mathbf{r}}^x \end{pmatrix}. \quad (25)
$$

Inserting this transformation into the continuous free energy density $\mathcal{F}$ in Eq. (2), and remembering to also transform the covariant gradients, it is readily verified that all terms are invariant under C_4 as indeed they need to be since $C_4 \in D_{4h}$. For the discretized xy-basis version of the same free energy in Eqs. (11)–(15), it is then similarly possible to check that all terms are invariant under C_4 except for the mixed gradient terms in Eq. (19). The reason why this term is not symmetric but the continuum version is, is again that the forward difference discretization procedure in Eq. (10) introduces artificial anisotropies in the system; usually referred to as lattice potentials and does not in general guarantee that the discretized version satisfies all continuum symmetries. In this particular case, it manifests as an explicit asymmetry because the gradients are in different directions in the same term.

Since all other terms than the mixed gradient terms are already symmetric w.r.t. C_4, it suffices to only present the rotated version of this particular term when calculating the symmetrized lattice free energy density $\mathcal{F}^s$. The details of this expression can be found in Appendix B.

E. Boundary conditions and Landau gauge

The gauge field link variables are split into a fluctuating and a constant part such that $A_{\mathbf{r},\mu} = A_{\mathbf{r},\mu}^f + A_{\mathbf{r},\mu}^c$. Periodic boundary conditions are used in the fluctuating part $A_{\mathbf{r},\mu}^f$, as well as in the discretized field components such that $\eta_{\mathbf{r}}^a = \eta_{\mathbf{r}+L_\mu}^a$. For the constant part $A_{\mathbf{r},\mu}^c$, twisted boundary conditions are used by employing the extended Landau gauge forcing a fixed magnetic flux through the system. The extended Landau gauge is given by

$$
A_{\mathbf{r},q}^c = \frac{2\pi m_q}{L_{\bar{q}}} r_{\bar{q}}, \quad A_{\mathbf{r},z}^c = 0, \quad (26)
$$

where $m_q \in \mathbb{Z}$ and the conditions in Refs. [54,55] have already been incorporated. This definition makes the full link

variable boundary conditions periodic modulo 2π, which prevents geometric frustration. Equation (26) together with periodic boundary conditions for $A_{\mathbf{r},\mu}^{f}$ forces the system to satisfy the property $\oint \mathbf{A} \cdot d\mathbf{r}_{\perp} = 2\pi f L_x L_y$. This gives a magnetic flux $\mathbf{B} = 2\pi f \hat{z}$ through the system for filling fraction

$$f = \frac{m_y}{L_x} - \frac{m_x}{L_y}. \tag{27}$$

The filling fraction then gives the number of magnetic field vortex quanta pr. plaquette in the xy plane. In the results presented in this paper the choice $m_y = 1, m_x = 0$, which reduces the gauge to the normal Landau gauge, has been used for a system with $L_x = L_y = 64$ which yields $f = 1/64$. The qualitative conclusions have however been tested for the symmetric choice $m_y = 1, m_x = -1$. This choice is symmetric in the sense that in this case we may write $\mathbf{A}^c = -\mathbf{r} \times \mathbf{B}/2$ for $\mathbf{B} = 4\pi/L\hat{z}$.

III. DETAILS OF THE NUMERICAL CALCULATIONS

A. Monte-Carlo update method

For the Monte-Carlo simulations, the Metropolis-Hastings method [56] was used to sample states with a probability distribution given by the free energy in Eq. (9). This method fulfills the detailed-balance criteria such that importance sampling gives thermodynamic averages as simple arithmetic averages over the sampled states [57–59]. This method, as well as all other numerics, was implemented in the Julia programming language [60] version 1.0.3.

As described in Sec. II B, the free energy was discretized on a cubic lattice of size $L_x \times L_y \times L_z$. Each lattice point contains one fluctuating variable for each of the xy-basis phases: $\theta_{\mathbf{r}}^x$ and $\theta_{\mathbf{r}}^y$, and three fluctuating link variables for the gauge field, one for each direction of space: $A_{\mathbf{r},x}$, $A_{\mathbf{r},y}$, and $A_{\mathbf{r},z}$. A Monte-Carlo update consists in this case of proposing new values of all these variables, which proposes a new state of a single lattice point and then rejecting or accepting this state according to the Metropolis-Hastings method. A Monte-Carlo sweep then consists of doing this for each individual lattice point. New values of the phases were proposed uniformly on an open interval $\theta_{\mathbf{r}}^x, \theta_{\mathbf{r}}^y \in [0, 2\pi)$ using the Julia rand() function which uses the Mersenne-Twister algorithm [61]. The gauge-field link variables were updated by a uniformly distributed random value $A_{\mathbf{r},q}'$ in a symmetric region centered on the previous value $A_{\mathbf{r},q}$, such that $A_{\mathbf{r},q}' - A_{\mathbf{r},q} \in [-A, A]$. The parameter A which sets the size of the region was set to $A = 0.1$ based on the fact that at this value at high temperature, the percentage of proposed states that were accepted was $\sim 30\%$.

In order to facilitate efficient computation on highly parallelized computer systems, the numerical lattice was divided into sublattices that communicated with each other as their lattice points were updated. The number of sublattices was chosen according to what gave the fastest average performance of Monte-Carlo sweeps, which for cubic systems of size $L = 64$ turned out to be 16 sublattices. A single MC sweep was then performed in, on average, 0.11 ± 0.01 s.

B. Observables

To study the model in Eq. (1) in the chiral basis, the xy-basis variables were converted into their chiral counterparts through Eq. (3). Since the trigonometric formulas for obtaining the chiral phases $\theta_{\mathbf{r}}^h$ diverge when $|\eta_{\pm}| \to 0$, these were expanded to fourth order to handle this case. The technical details of this can be found in Appendix C.

To characterize the vortices, we calculate the curl of the gauge-invariant phase difference of each chiral component, namely $(\nabla \times (\nabla \theta^h - \mathbf{A}))/2\pi$. This amounts to calculating the lattice curl of the gauge-invariant phase difference $\Delta_q \theta_{\mathbf{r}}^h - A_{\mathbf{r},q}$ around a fundamental plaquette of the numerical lattice. By adding the constant magnetic flux density f, we obtain a quantity which we will call the local vorticity of each component [53]

$$n_{\mathbf{r},z}^h = \frac{1}{2\pi} \epsilon_{zij} \Delta_i \left(\Delta_j \theta_{\mathbf{r}}^h - A_{\mathbf{r},j} \right)_{\pi} + f, \tag{28}$$

where implicit summation over indices is understood and ϵ_{zij} is the Levi-Civita symbol. $(\phi)_{\pi}$ is shorthand notation for $\mod(\phi + \pi, 2\pi) - \pi$, which draws the argument back into the primary interval $[-\pi, \pi)$. The filling fraction f is defined in Eq. (27) and gives the number of fundamental vortex quanta pr. planar plaquette as determined by the extended Landau gauge [53,62,63]. Note that $\Delta_q \theta_{\mathbf{r}}^h - A_{\mathbf{r},q}$ in general does not give the current of each component in the p-wave case, but is sufficient to distinguish the structure of vortices and to compare with the results in Ref. [39]. The z-averaged vorticity is then naturally defined as

$$n_{\mathbf{r}_{\perp},z}^h = \frac{1}{L_z} \sum_{r_z=0}^{L_z-1} n_{\mathbf{r},z}^h, \tag{29}$$

which is used through its thermal average $\langle n_{\mathbf{r}_{\perp},z}^h \rangle$ in order to obtain detailed information about the real space structure of the vortex lattices as well as of the vortex cores in the present model.

A related observable is the z-averaged gauge invariant chiral phase difference

$$\delta\theta_{\mathbf{r}_{\perp}} = \left\langle \frac{1}{L_z} \sum_{r_z=0}^{L_z-1} (\theta_{\mathbf{r}}^+ - \theta_{\mathbf{r}}^-)_{\pi} \right\rangle, \tag{30}$$

where $\langle \cdot \rangle$ denotes thermal averaging. This observable is also useful in studying the nature of the vortices.

To extract a clearer picture of the overall spatial correlations of the vortex lattice we define the structure function

$$S^h(\mathbf{k}_{\perp}) = \frac{1}{(f L_x L_y)^2} \left\langle \left| \sum_{\mathbf{r}_{\perp}} n_{\mathbf{r}_{\perp},z}^h e^{i\mathbf{k}_{\perp} \cdot \mathbf{r}_{\perp}} \right|^2 \right\rangle, \tag{31}$$

which essentially amounts to taking the planar Fourier transform of the z-averaged vorticity. The fast-Fourier algorithm was used to efficiently compute the structure function for all Bragg points $\mathbf{k}_{\perp}$. The structure function is normalized such that $S^h(\mathbf{0}) = 1$.

For any vortex lattice signature, the structure function is expected to exhibit peaks at characteristic Bragg points situated equidistantly from the origin. For a hexagonal lattice we expect six peaks with $\pi/3$ mutual angular distance, while

for a square lattice we expect four peaks with $\pi/2$ mutual angular distance. To distinguish these two signals clearly, the histogram

$$h(\delta\Delta\phi^h) = \frac{1}{\delta\Delta\phi^h \left|\{\Delta\phi_i^h\}\right|} \sum_{\{\Delta\phi_i^h\}} \delta_{\Delta\phi_i^h \in \delta\Delta\phi^h} \qquad (32)$$

is constructed, where $\delta\Delta\phi^h$ is some angular interval bin. The angular distances $\Delta\phi_i^h$ are obtained by calculating $S^h(\mathbf{k}_\perp)$ using a certain number of Monte-Carlo measurements, then finding the radius $|\mathbf{k}_\perp|_m$ which yields the largest value of $\int_0^{2\pi} S^h(|\mathbf{k}_\perp|, \phi)d\phi$. A ribbon is then constructed around this radius from which the largest value of $S^h(\mathbf{k}_\perp)$ is picked for each angle such that

$$S^h(\phi) = \max\{S^h(|\mathbf{k}_\perp|, \phi) \ : \ ||\mathbf{k}_\perp| - |\mathbf{k}_\perp|_m| < k_r\}. \quad (33)$$

The angular positions $\{\phi_i\}$ of the six highest peaks in $S^h(\phi)$ are then found. Finally all mutual distances between these positions are found $\{\Delta\phi_i\} = \{|\phi_k - \phi_j| \ : \ \phi_k < \phi_j\}$ which is used to calculate the histogram $h(\delta\Delta\phi^h)$. The process is repeated for independent Monte-Carlo measurements of $S^h(\mathbf{k}_\perp)$ until there are sufficient $\Delta\phi_i$ to construct the histogram.

The above quantities, taken together, provide considerable information on not only the symmetry of the vortex lattices at various temperatures but also on the structure of the vortex cores corresponding to each lattice symmetry. The critical temperature at the position of the upper critical field crossover line $H_{c2}(T)$ was found by examining the specific heat

$$C_v = \beta^2\big(\langle E^2\rangle - \langle E\rangle^2\big) \qquad (34)$$

and a chiral order parameter that we will now describe. The Higgs field components η^+ and η^- are related through the time-reversal transformation, hence a difference in their density signify a spontaneous breaking of $\mathbb{Z}_2$ time-reversal symmetry. Since this density can be measured by the component amplitudes, a useful chiral order parameter is given by

$$\delta u^2 = \left| \left\langle \frac{1}{L_x L_y L_z} \sum_\mathbf{r} \left(\rho_\mathbf{r}^{+\,2} - \rho_\mathbf{r}^{-\,2}\right) \right\rangle \right|$$
$$= \frac{2\rho^x \rho^y}{L_x L_y L_y} \left| \left\langle \sum_\mathbf{r} \sin\left(\theta_\mathbf{r}^x - \theta_\mathbf{r}^y\right) \right\rangle \right|. \qquad (35)$$

From the last line it is clear that it is the locking of the xy phase difference that is responsible for the breaking of time-reversal symmetry.

C. Thermalization and measurement steps

Before measurements of observables were performed, the lattice was initialized with random values for all fluctuating variables at each lattice point, resulting in high energy states. Then, a two-step thermalization procedure was done which consisted of a stepwise decrease in temperature to decrease the chance of a metastable state, followed by a number of basic Monte-Carlo sweeps (thermalization). The steps during the cooldown procedure were distributed as a geometric series between a high and low temperature, so that more MC sweeps would be concentrated at lower temperatures. During cooldown, $\approx 1.3 \times 10^5$ MC sweeps were distributed

equally on 1024 temperature steps. This was then followed by $\approx 1.3 \times 10^5$ additional MC sweeps that were discarded before measurements began. To confirm that this yielded a properly thermalized state, we checked that the internal energy of the system as a function of MC time had converged and remained stable during measurements.

256 intermediate MC sweeps were performed between each measurement to diminish autocorrelation effects. The number of measurements of observables varied between simulations, from 1024 for sampling at high temperatures, to 4096 when estimating C_v close to the phase transition.

Measurements were performed sequentially by lowering the temperature, such that the last state of the lattice in the measurement series at one temperature was used as the initial state when thermalizing the simulation for the next lower temperature. To prevent the simulation from getting stuck in a metastable state, several series of simulations were performed using independent initial states to verify the validity of the results.

D. Post-processing

Multihistogram Ferrenberg-Swendsen reweighting [64,65] was used to calculate the specific heat C_v accurately at temperatures close to the peak in C_v. The nonlinear Ferrenberg-Swendsen equations for free energy were solved self-consistently and iteratively using the Julia NLsolve library in which automatic forward differentiation was used to find the Jacobian and a trust-region method was used as the iterative algorithm [66].

The jackknife method [67] and Ferrenberg-Swendsen reweighting [64,65] were used to compute averages and uncertainties of observables. The number of blocks dividing the measurement series in the jackknife method was set to 128. This gave a block length where the estimate of variance had leveled off, indicating that autocorrelations had effectively been reduced.

IV. LATTICE STRUCTURES

Before we present our numerical results based on our large-scale Monte-Carlo simulations, we provide a schematic introduction to the results to assist the reader. In Fig. 2, we show schematically vorticities and phase windings that we expect to find for two different types of vortices. In the following, the notation will be as follows. A phase winding in chiral component η_+ of $2\pi n_+$ and in chiral component η_- of $2\pi n_-$ will be denoted (n_+, n_-). A vortex with $(n_+, n_-) = (1, -1)$ will be denoted as singly quantized. A vortex with $(n_+, n_-) = (2, 0)$ will be denoted as doubly quantized.

For a singly-quantized vortex, the vorticity is expected to have a magnetic field-profile centered at the origin, with a maximum magnetic field at the origin, see Fig. 2(a). The corresponding phase winding is shown in Fig. 2(c). Note the fourfold symmetry in the color pattern, the radial monotonicity in the phase value away from the origin, and the 2π discontinuity along the horizontal axis. For a doubly-quantized vortex, the vorticity is expected to have a magnetic field profile centered at the origin, with a minimum magnetic field at the origin and a ring of maxima away from the origin,
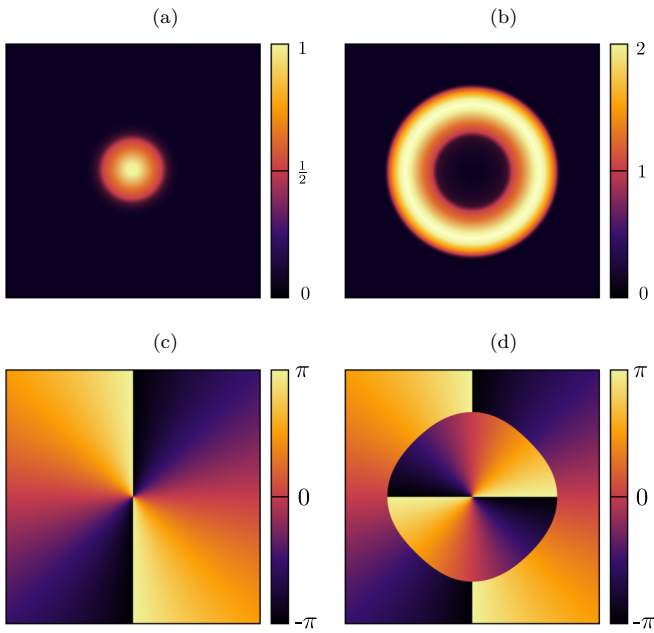
FIG. 2. Schematic of vorticities and corresponding phase difference signature $\theta^+ - \theta^-$ of vortices for $H > 0$. (a) and (c) shows vorticity and phase difference, respectively, for a singly-quantized vortex with winding number $n_+ = 1$ and $n_- = -1$. (b) and (d) shows vorticity and phase difference, respectively, for a doubly-quantized vortex with winding number $n_+ = 2$ and $n_- = 0$. The figures are directly based on the ones presented in Ref. [39].

see Fig. 2(b). The corresponding phase winding is shown in Fig. 2(d). The main difference from the phase winding in Fig. 2(c) is the inner circle close to the origin, where phase windings are rotated by $\pi/2$ compared to the phase windings in Fig. 2(c). For a detailed discussion of this point, see also Sec. III of Ref. [39].

This will be our main diagnostic tool for identifying whether vortices are singly or doubly quantized. As a check on this, we will count the total vorticity in each component and check that this corresponds to the total vorticity of the system, given by the external magnetic field.

In the following, we focus on results obtained for the parameter set $\nu = 0.1$, $g = 0.3$, $f = 1/64$. The parameter $\nu = 0.1$ corresponds to a moderately fourfold anisotropic Fermi surface. To set the temperature scale of our finite-field simulations, we have found it useful to first perform Monte-Carlo simulations in zero field to locate the maximum of the specific heat C_v. This maximum occurs at $T \approx 2.016 \pm 0.002$ for $f = 0$, which we denote as the critical temperature T_c of the superconductor. A rounded and suppressed peak in the specific heat persists at $f > 0$. For $f = 1/64$, this rounded peak (no longer a phase transition) occurs at $T = 1.86 \pm 0.04$. $T = 1.86$ is therefore a natural temperature scale for the vortex system at $f = 1/64$. For this filling fraction, we only expect to see vortex lattice structures for $T < 1.86$.

We will mainly present results starting with high temperatures and then proceeding to lower temperatures. At high temperatures, we will find a plasma phase totally dominated by thermally induced vortex loops. Proceeding to lower temperatures where a vortex-lattice forms, we find a singly-

quantized square vortex lattice. Lowering the temperatures further, we eventually find a doubly-quantized hexagonal lattice. At the end, we briefly discuss a "mixed" phase of singly-quantized and doubly-quantized vortices, located at intermediate temperature between the doubly-quantized and singly-quantized vortex lattice phases.

A. Specific heat and chiral order parameter

To investigate what the relevant temperature scale in our system is, we have performed Monte-Carlo simulations computing the specific heat and chiral order parameter at $f = 0$ and $f = 1/64$. Figure 3 shows the specific heat as a function of temperature at $f = 0$. A sharp peak is seen at a temperature $T = 2.016 \pm 0.002$ and marks the phase transition from the superconducting to the normal state. Also shown is the specific heat at $f = 1/64$, which at $T^* = 1.86 \pm 0.04$ shows a broadened and suppressed peak compared to $f = 0$. This peak marks the finite-field crossover to the normal state. In what follows we will refer to this crossover temperature as $T^*(f)$.

The inset shows the chiral order parameter as a function of T at $f = 0$ and $f = 1/64$. For $f = 0$, it vanishes at the same temperature as the sharp peak in the specific heat is located and shows that the $f = 0$ phase transition in this model is associated with spontaneous time-reversal symmetry breaking. For $f = 1/64$, the presence of a magnetic field explicitly breaks time-reversal symmetry by selecting a preferred chirality, which leads to a finite order parameter at $T^*(f)$.

These results form a useful background for choosing relevant temperatures at which to study vortex-lattice states at finite f. Below, we will study such vortex states in the temperature regime $T \in [1.5\text{–}1.8]$, and from the above results we conclude that these represent significant temperatures on the scale of the critical temperature T_c. Hence, our Monte-Carlo simulations at such temperatures will yield useful information concerning the thermal stability of the vortex states we find.

B. Vortex states upon lowering temperature

1. Plasma state

For $f = 1/64$ and at high temperatures $T \gtrsim 1.90$, the superconductor is in a normal state where thermal fluctuations have induced a proliferation of massive amounts of closed vortex loops in the system. The resulting state is therefore a vortex-plasma phase. This leads to the tableau shown in Fig. 4, which depicts results of simulations at $T = 2.0$. The uniform distribution of vorticity in space leads to a circular pattern at low k-vector magnitude with increasing value with increasing magnitude of the k vector. At higher k-vector magnitude, the value of the structure function exhibits a square anisotropy with higher values close to $\mathbf{k}_{\text{corners}} = \pi(1 - 2n, 1 - 2m)$ for $n, m \in \{0, 1\}$. This anisotropy is due to short range correlations since as $\mathbf{k}$ approaches $\mathbf{k}_{\text{corners}}$, $\mathbf{k}$ measures shorter and shorter correlations because of periodic boundary conditions. At these length scales, the quadratic numerical lattice upon which the continuum model has been discretized gains significance and leads to the apparent anisotropy. The limits of the color bar reveal that this anisotropy is very small, with a maximum value less than 0.010. There is no real signal of
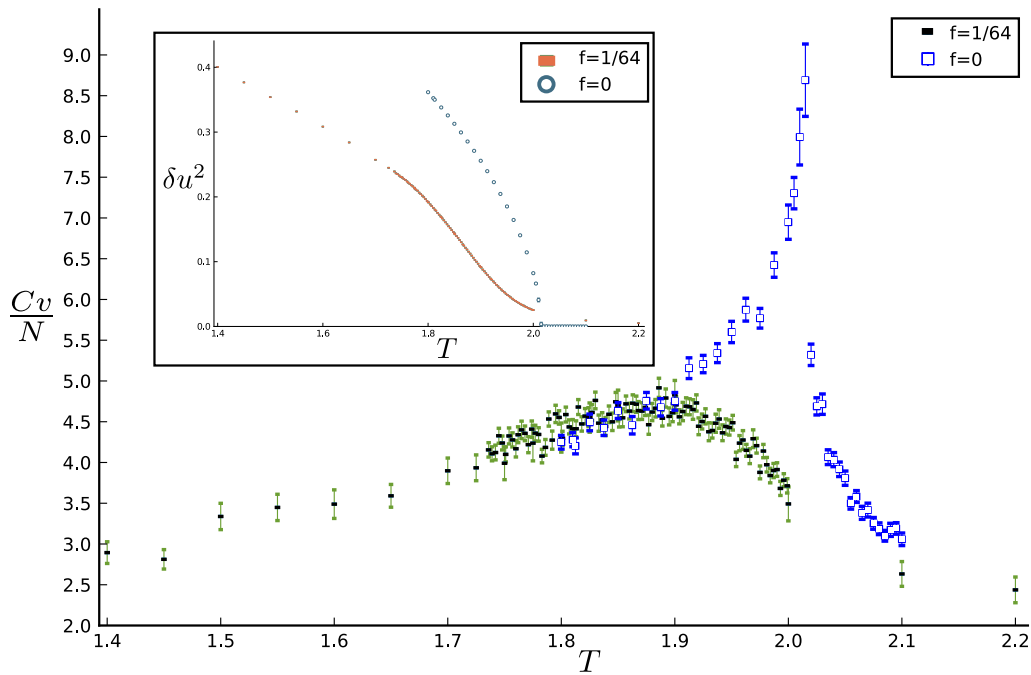
FIG. 3. Specific heat dependence on temperature for a system with $g = 0.3$, $v = 0.1$, and $L = 64$. The blue points marked by a hollow square are for $f = 0$, while the green dataset with points marked by a black dash is for a system with $f = 1/64$. The inset shows the chiral order parameter δu^2 for the two filling fractions $f = 0$ and $1/64$, with azure circles showing $f = 0$ while orange dashes show $f = 1/64$. In the inset, the error bars are for the most part too small to be seen.
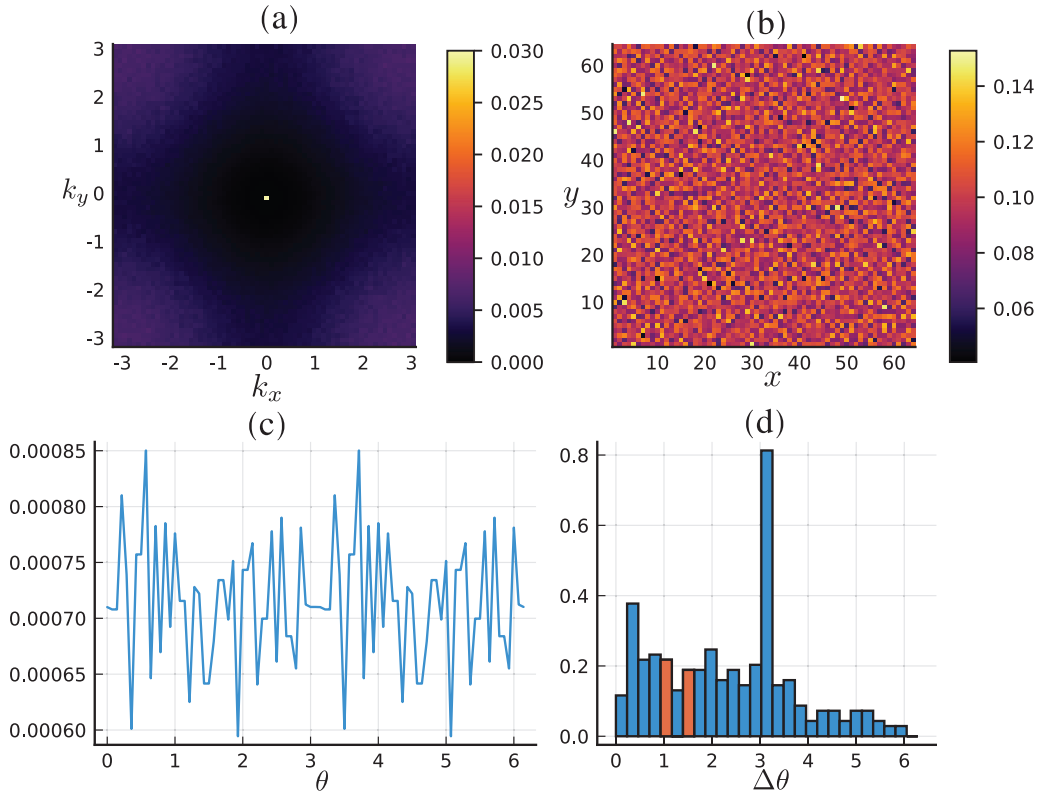

FIG. 4. Vortex state at $T = 2.0$ for a system with $v = 0.1$, $g = 0.3$, and $f = 1/64$. The system is dominated by thermally induced vortices. (a) Thermal average of the structure function. (b) Thermal average of real space vorticity. (c) Angular dependence of the structure function in a circular thin annulus around $\mathbf{k} = 0$. (d) Histogram of angular difference $\Delta\theta$ between peaks in the angular dependence of the structure function. The colored bars are the bins that include $\Delta\theta = \pi/3$ and $\Delta\theta = \pi/2$. These would correspond to hexagonal and square lattices, respectively.
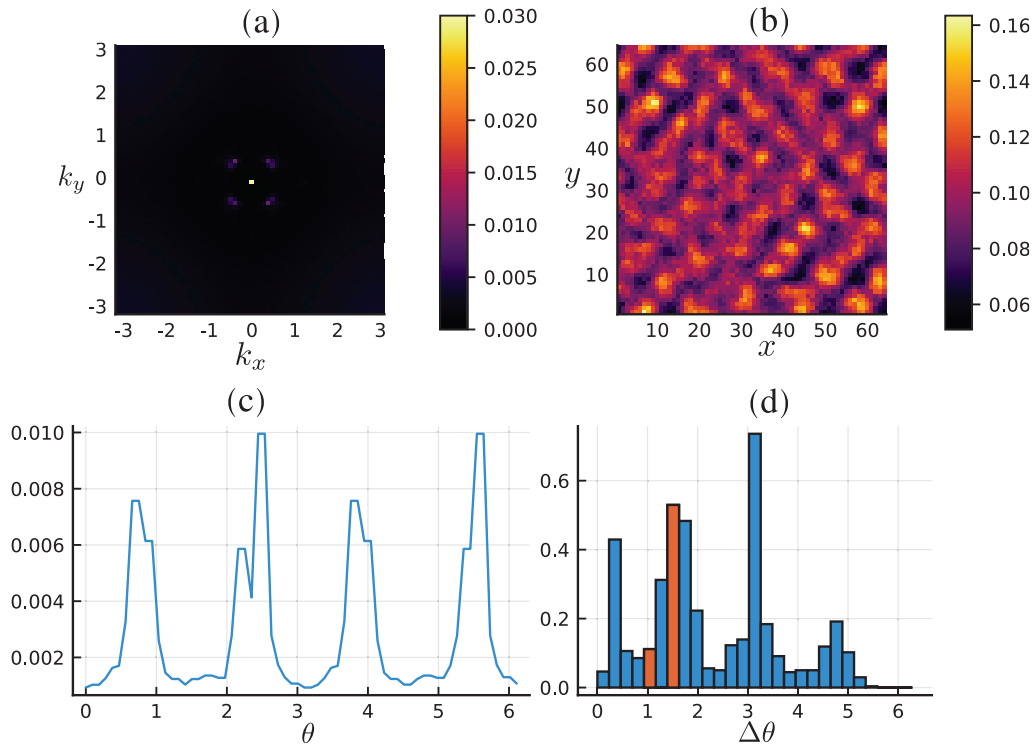
FIG. 5. Singly-quantized square vortex lattice state for a system with $\nu = 0.1$, $g = 0.3$, $f = 1/64$, and $T = 1.786$. (a) shows the structure function of a square vortex lattice. (b) shows the vortex lattice structure in real space. The vortices are located at the bright spots. All vortices have a field maximum at the center of the vortex, cf. Fig. 2(a), consistent with singly-quantized vortices. (c) shows the fourfold angular distribution of the structure function. (d) shows a histogram of the angular difference between peaks in the structure function. The colored histograms denote angular difference between peaks in the structure functions corresponding to $\pi/3$ and $\pi/2$. The dominant peaks are found at $\Delta\theta = \pi/2, \pi$, and $3\pi/2$, corresponding to a square lattice.

vortex-lattice correlations detected at this temperature. The histogram in Fig. 4(d) reveals a large spike at $\Delta\theta = \pi$. This originates with the fact that the Fourier transform has the property $\mathcal{F}(\mathbf{k}) = \mathcal{F}(-\mathbf{k})^*$, such that the structure function is equal at $\mathbf{k}$ and $-\mathbf{k}$.

2. Singly-quantized square vortex lattice

We next discuss the vortex lattice state that first emerges as the temperature is lowered below the crossover temperature to the normal state, which is $T^* = 1.86$ at $\nu = 0.1$, $g = 0.3$, and $f = 1/64$. Figure 5 shows the results of Monte-Carlo simulations performed at $T = 1.786$, computing the structure function (a), vorticities (b), angular distribution of peaks in the structure function (c), and histograms of angular difference between peaks in the structure function (d). The structure function clearly has fourfold symmetry, such that the vortex lattice is square. This is also discernible in panel (b), although less obvious than in (a). The angular dependence of the structure function shown in (c) shows four clear peaks separated by $\pi/2$. The histograms of $\Delta\theta$ in (d) show that the most dominant nontrivial bin is $\pi/2$, marked by the orange bar. The broadening around the large orange bar is due to thermal fluctuations. The smaller orange bar represents the counts at angular difference of $\pi/3$, corresponding to a hexagonal lattice. The square lattice peak dominates the hexagonal peak, leading to the conclusion that the symmetry of the lattice is square, consistent with the result for the structure function in

(a). The peak in (d) at low angular value is attributed to the square lattice peaks being jagged due to the temperature being close to T_c.

Figure 5(b) shows the square lattice structure as a real space average. One notable feature of the results of Fig. 5, apart from the square vortex-lattice structure shown in (a), is that the magnetic field maximum associated with the vortices in (b) are located at the center of the vortices. Referring back to our discussion of Fig. 2, we see that this is consistent with singly-quantized vortices in each chiral component ($n_+ = 1, n_- = -1$).

The nature of these points of increased vorticity is investigated further by comparing the position of these points with a real-space plot of average local phase difference between the two components: $\langle \theta_\mathbf{r}^+ - \theta_\mathbf{r}^- \rangle$ in Fig. 6. The figures show that points of increased vorticity correspond well with intersections between two regions of positive average phase difference and two regions of negative average phase difference. This corresponds to the same phase-difference pattern that is depicted in Fig. 2(c), again characteristic of singly-quantized vortices.

The single quantum nature of the vortices is further corroborated by the fact that the boundary conditions enforce a total of 64 quanta of magnetic flux at any step of the Monte-Carlo simulations. In Fig. 5, there are 62 clearly identifiable points of increased vorticity. It could be that the system shows 62 single-quanta vortices and the remaining two vortices are too thermally distorted to form enough of a coherent thermal
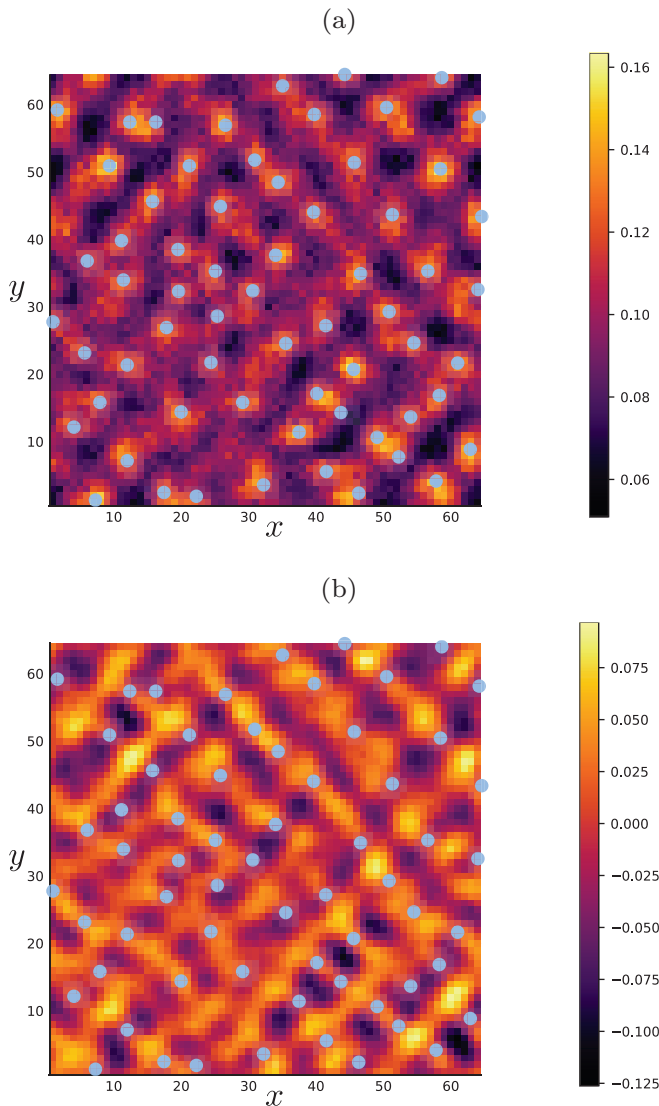
(a)

(b)

FIG. 6. Vortex positions and phase differences for the parameters used in Fig. 5. (a) shows an enhanced version of Fig. 5(b). The center of each vortex is marked by a green dot. The azure dots mark the positions of increased vorticity in the real space average. This corresponds to a maximum of the magnetic field at the center of the vortex, cf. the schematics of Fig. 2(a). (b) shows the phase difference around each vortex, whose position is indicated by a green dot. Note the fourfold symmetry of the phase-difference pattern around the vortices, cf. the schematics of Fig. 2(c). (a) and (b) corroborate, along with the results of Fig. 5, that at $(f = 1/64, T = 1.786)$ the vortex lattice is a singly-quantized square lattice.

average to be identified, or it could be that the system has 60 single quanta vortices and two double-quanta vortices. In any case, it is clear that the vortex state is dominated by singly-quantized vortices.

The superconducting field amplitude of conventional superconductors is suppressed in the presence of vortices. In the case of a two-component field, the subdominant component may be induced in the vicinity of the vortex core where the dominant component is suppressed [39]. This is evident in Fig. 7 where the dominant component amplitude ρ^+ on the left exhibits dark regions that correspond to the location of

increased vorticity in Fig. 5(b) and Fig. 6(a). On the right, the subdominant component exhibits increased amplitude in these regions as is required by the pseudo-$\mathbb{CP}^1$ constraint in Eq. (21). We conclude from this that the stable vortex state at $\nu = 0.1, g = 0.3, f = 1/64, T = 1.786$ is a singly-quantized square vortex lattice.

3. Doubly-quantized hexagonal vortex lattice

We next consider the system at $f = 1/64$ and a lower temperature $T = 1.5$. The plot of the average structure function in Fig. 8(a) shows six clear, equidistantly placed peaks. Figure 8(b) shows the average vorticities in real space. The vorticity distribution around each vortex is clearly of the same type as depicted in Fig. 2(b), characteristic of doubly-quantized vortices. The angular dependence of the structure function in a thin annulus around $\mathbf{k} = 0$ is shown in Fig. 8(c), where six clear equidistantly placed peaks are seen. This is again reflected in the histogram for $\Delta\theta$ in Fig. 8(d) where a large peak is observed at $\Delta\theta = \pi/3$ followed by peaks at integer multiples of this. The real space vorticity average shows 32 independent ring structures (note that periodic boundary conditions have been used), which indicates that each structure has two quanta of magnetic flux.

Figure 9(a) shows an enhanced version of Fig. 8(b). The ringlike structure of enhanced vorticity surrounding the center of each vortex is clearly seen, consistent with what is depicted in Fig. 2(b). This is indicative of doubly-quantized vortices $(n_+ = 2, n_- = 0)$. The double quantum nature of the vortices is also observed in the plot of real space phase difference average in Fig. 9(b). It shows a clear inner 4π phase change at low radius from the vortex center, where positive phase difference is observed at an angle $\pi/4$ and $5\pi/4$ from the vortex center and negative phase difference at $3\pi/4$ and $7\pi/4$. This pattern is repeated at larger radii away from the vortex core but then rotated by $\pi/2$ degrees giving the vortices a distinct core structure not observed in the single-quantum case. It is finally noted that the real space average vorticity in Fig. 8 shows decreased vorticity in the vortex core for the positive component.

The component amplitudes in Fig. 10 again reflect the hexagonal lattice pattern in Figs. 8 and 9. The dominant component on the left is clearly seen to be suppressed in the vicinity of the vortex cores, while the amplitude plot of the subdominant component on the right shows that this component in coincidentally induced.

The conclusion is thus that the simulations at $f = 1/64, T = 1.5$ clearly show a hexagonal lattice of doubly-quantized vortices. Our simulations show that these doubly-quantized vortex states remain stable down to the lowest temperatures we have considered and persist up to temperatures of $T = 1.7$. The temperature regime $T \in [1.7$–$1.75]$ will be discussed further below.

4. Mixed doubly and singly quantized vortex lattices

We next discuss the temperature regime where the transition from a higher-temperature singly-quantized square vortex lattice to a lower-temperature doubly-quantized hexagonal vortex lattice takes place. For $f = 1/64$, the transition takes place in the narrow range $T \in [1.73$–$1.775]$. Recall
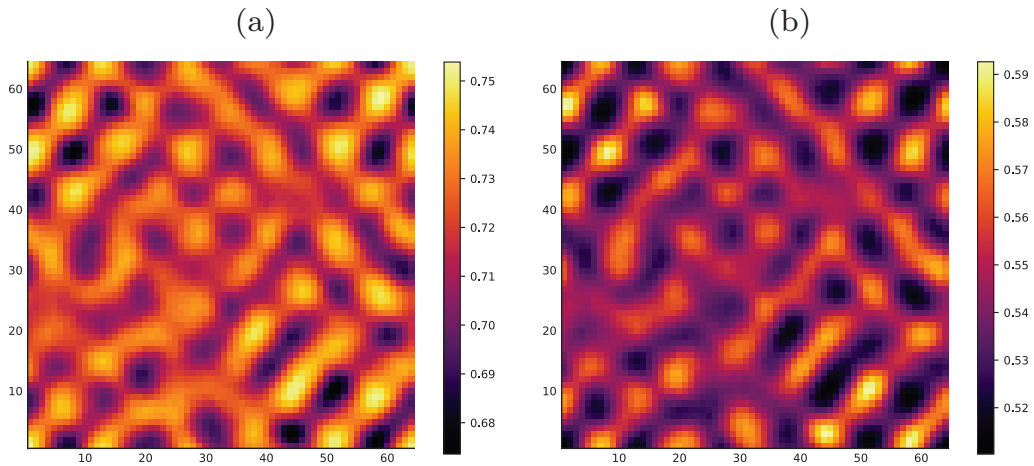
(a)   (b)

FIG. 7. Component amplitudes averaged in the z direction for a system with $\nu = 0.1$, $g = 0.3$, $f = 1/64$, and $T = 1.786$. (a) shows $\langle \rho^+_{\mathbf{r}_\perp} \rangle$ while (b) shows $\langle \rho^-_{\mathbf{r}_\perp} \rangle$. The color limits are set to amplify the spatial dependence, but we note that the average of ρ^+ is significantly higher than ρ^-.

that the zero-field transition takes place at $T_c = 2.016$ and the crossover temperature to the normal state at $f = 1/64$ is $T \approx 1.86$. The four tableaus in Fig. 11 show examples of states of the system at intermediate temperatures $T = 1.7, 1.725, 1.742, T = 1.751$.

At $T = 1.7$ and $T = 1.725$, the dominant structure is a doubly-quantized hexagonal vortex lattice. The structure function of the vortex lattice is predominantly hexagonal, see
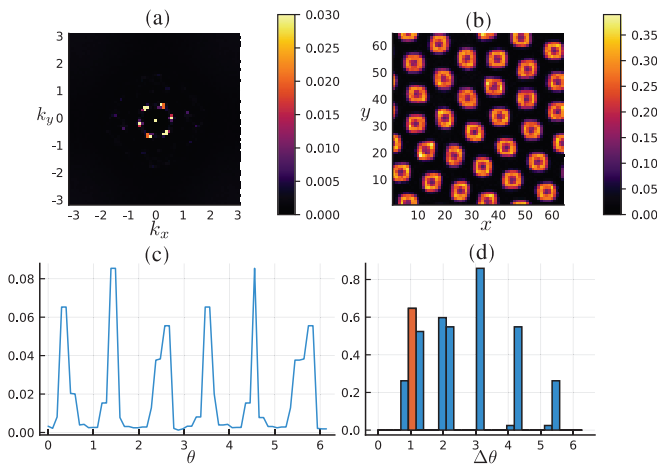

FIG. 8. Doubly-quantized hexagonal vortex lattice state for a system with $\nu = 0.1$, $g = 0.3$, $f = 1/64$, and $T = 1.5$. (a) shows the structure function, showing a hexagonal lattice. (b) shows the lattice structure in real space. Vortices are located at the dark spots surrounded by a bright ring. All vortices have a vorticity maximum distributed in a ring around the center of the vortex, and a careful count shows that there are 32 such doubly-quantized vortices, consistent with the system size $L_x \times L_y = 64 \times 64$ and $f = 1/64$. This vortex distribution is to be compared with the schematics of the upper right panel of Fig. 2. (c) shows the sixfold angular distribution of the structure function. (d) shows a histogram of the angular difference between peaks in the structure function. The colored histogram corresponds to an angular difference between peaks in the structure function of $\pi/3$. We see that the dominant peaks are found at $\Delta\theta = \pi/3$ and $2\pi/3$, which corresponds to a hexagonal lattice.

Figs. 11(a) and 11(e), but note the weakening of four of the peaks in the structure function in Fig. 11(e) compared to 11(a). $\langle n^h_{\mathbf{r}_\perp, z} \rangle$ in Figs. 11(b) and 11(f) shows vortices characterized by a center with low vorticity surrounded by a ring of higher vorticity. In this background, vortex structures start to appear that have a center of high vorticity, characteristic of singly-quantized vortices. Increasing the temperature further, the hexagonal pattern in the structure function is gradually replaced by a square pattern.

At $T = 1.742$, the structure function features two strong peaks at opposite wave vectors, with two weaker peaks in the orthogonal directions. The overall symmetry of the structure function is now closer to one characteristic of a square lattice, see Fig. 11(i). Namely, the four weaker spots in the sixfold symmetric structure functions in Figs. 11(a) and 11(e) have moved closer to each other. Although there is still a considerable number of doubly-quantized vortices present, i.e., vortices with low vorticity at the center surrounded by a ring of higher vorticity, it is evident that a substantial number of singly-quantized vortices have appeared, see Fig. 11(j).

Increasing the temperature slightly to $T = 1.751$, this becomes more pronounced. In Fig. 11(m), the fourfold symmetry of the structure function is evident, while Fig. 11(n) shows that there are still doubly-quantized vortices present. The transition from hexagonal to square vortex lattices upon increasing the temperature from $T = 1.7$ to $T = 1.75$ is mirrored in the peak-distance histogram with the bin at $\Delta\theta = \pi/3$ losing value and eventually being superseded by the bin at $\Delta\theta = \pi/2$, see Figs. 11(c), 11(g), 11(k), and 11(o), as well as Figs. 11(d), 11(h), 11(l), and 11(p).

For a clearer picture of the temperature range over which this transition happens, we have computed the temperature dependence of these two histogram bins, shown in Fig. 12. The bin at $\Delta\theta = \pi/3$ (hexagonal vortex lattice) clearly dominates at lower temperatures and becomes equal in height to the bin at $\Delta\theta = \pi/2$ (square vortex lattice) at $T \approx 1.75$. The temperature dependence of the two bins mirrors the dissociation of double quanta vortices into single quanta vortices which we have noted is already starting at $T \approx 1.7$. The histogram bins approach the value $h^+(\delta\Delta\theta) = 1/2\pi$ after the $U(1)$ crossover
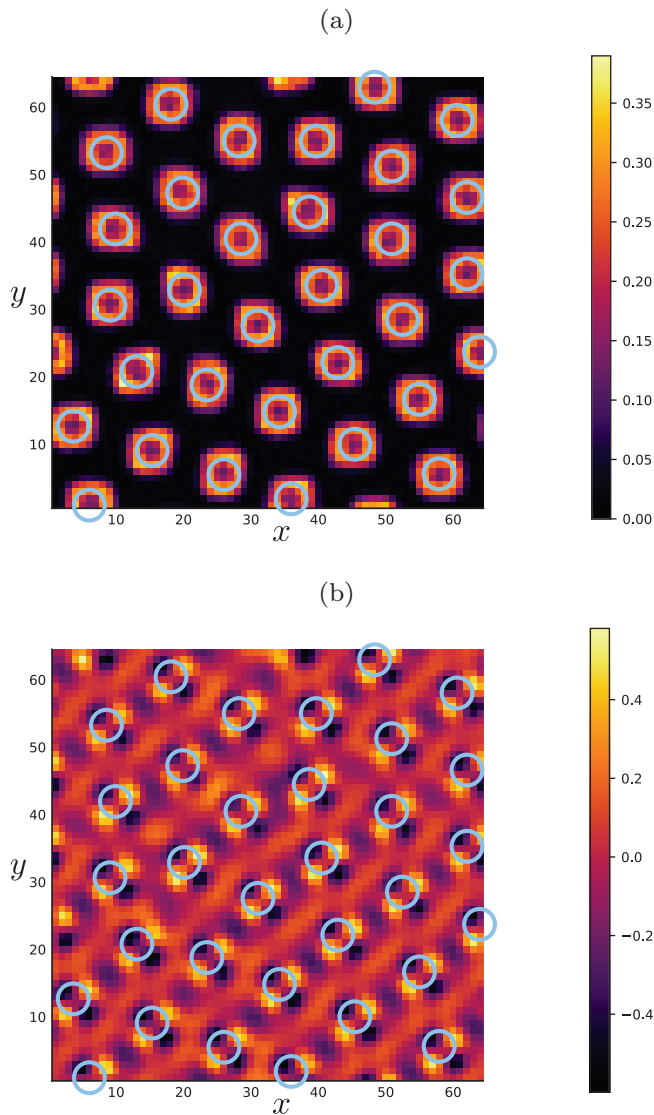
(a)

(b)

FIG. 9. Phase difference and $+$ vorticity of the system in Fig. 8. The blue circles represent rings with increased vorticity in (a). These rings are then overlaid on the real space average of phase difference in (b).

transition, which is an equal weight of the histogram on all bins. The lack of angular variations in the structure function means that the system is in the vortex plasma phase.

The temperature regime in which the lattice reconstruction takes place is thus rather narrow and close to the $H_{c2}(T)$ crossover line. This is consistent with previous computations that ignored thermal fluctuations [39], where the transition was induced by increasing the strength of the magnetic field up to values close to H_{c2}.

V. COMPARISON WITH MEAN-FIELD THEORY

Figure 12 gives a precise indication of where the vortex-lattice melting temperature in this system is, which is the temperature at which the two bins approach equal values and above which their values remain constant. This occurs at $T^* \approx 1.88$, only slightly above the estimated T where the broad

peak in the specific heat is located at $T = 1.86$. The temperature window for which a square singly-quantized vortex lattice dominates is therefore conservatively estimated to be in the range $T \in [1.75–1.86]$. Below $T = 1.7$, a doubly-quantized hexagonal vortex lattice is stabilized. Using the melting temperature as a measure of the transition to the normal state, i.e., as a measure of the upper critical field line, we see that the hexagonal lattice of double-quanta vortices is stable up to a temperature of about $0.9T^*$.

We now compare these results quantitatively with previously found mean-field results, where entropic effects were not fully accounted for [39]. Figure 13 displays three qualitatively different vortex phases obtained from simulations of mean-field theory in an external field at various temperatures. The procedure is to discretize the physical degrees of freedom $\eta_\pm$, and **A** using a finite-element framework, and to numerically minimize the free energy (1d) in an external magnetic field (for details, see Ref. [39]).

The mean-field temperature is accounted for by modifying the quadratic term of the potential (1d) to be $(T_{\mathrm{MF}} - 1)|\eta_h|^2$. There, the zero-field critical temperature is $T_{c,\mathrm{MF}} = 1$, and the crossover line to the normal state at $f_{\mathrm{MF}} \approx 1/30$ is estimated from our numerical results to be $T^*_{\mathrm{MF}} = 0.9$. For a better comparison of the role of the temperatures for the fluctuating theory with that of the mean field, the results of the temperatures for mean-field simulations are expressed in units of the crossover temperature T^*_{MF}.

At low temperatures, the minimal energy state is clearly a hexagonal lattice of double-quanta vortices. When approaching the crossover temperature, the double-quanta vortices start to split into single-quanta vortices. Around $0.86T^*_{\mathrm{MF}}$, there are few single quantum vortices, and the double quanta still dominate. Closer to the crossover, around $0.92T^*_{\mathrm{MF}}$, most of the vortices have dissociated and the single quantum vortices dominate. Eventually, the entire hexagonal lattice of double-quanta vortices has dissociated into a structure of single-quanta vortices. A generous estimate gives that the range of the mean-field temperature where the single-quanta vortices dominate is about $0.1T^*_{\mathrm{MF}}$. In general the entropic effects promote stability of the lattice of single-quanta vortices. However, our Monte-Carlo simulations demonstrate that in the regime of parameters we have considered, the double-quanta vortex lattice is robust in a regime of temperatures approximately equal to what was found in previous work [39].

VI. SUMMARY

In this paper, we have considered effects of thermal fluctuations on the vortex states in a model of a chiral p-wave superconductor with two complex matter fields (η^+, η^-) with opposite chiralities, for a filling fraction of $f = 1/64$ vortices per square plaquette in the (x, y) plane of a cubic numerical lattice, with an applied magnetic field in the z direction. We have considered temperatures in the interval $T \in 1.5–2.0$, with the zero-field critical temperature ($f = 0$) estimated to be $T_c = 2.016 \pm 0.002$ and the crossover line to the normal state at $f = 1/64$, estimated to be $T^* = 1.86 \pm 0.04$.

At $T = 1.5$ we have found that the stable field-induced vortex configuration is a hexagonal vortex lattice of doubly-quantized vortices. At the higher temperature $T \approx 1.75$, this
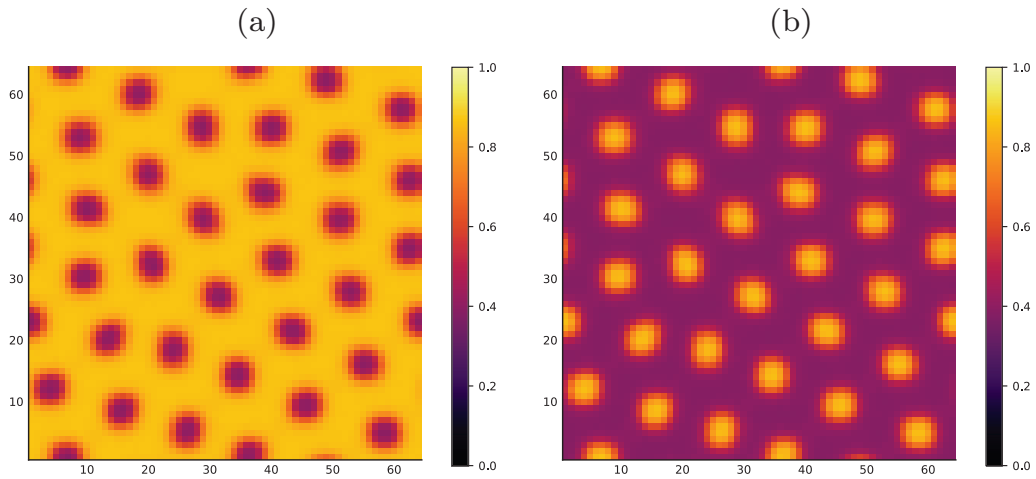
FIG. 10. Component amplitudes averaged in the z direction for a system with $\nu = 0.1$, $g = 0.3$, $f = 1/64$, and $T = 1.5$. (a) shows $\langle \rho_{\mathbf{r}_\perp}^+ \rangle$ while (b) shows $\langle \rho_{\mathbf{r}_\perp}^- \rangle$. In contrast to Fig. 7 the color limits are the same in both subplots since the lower temperature signal does not require amplification to discern spatial variance.
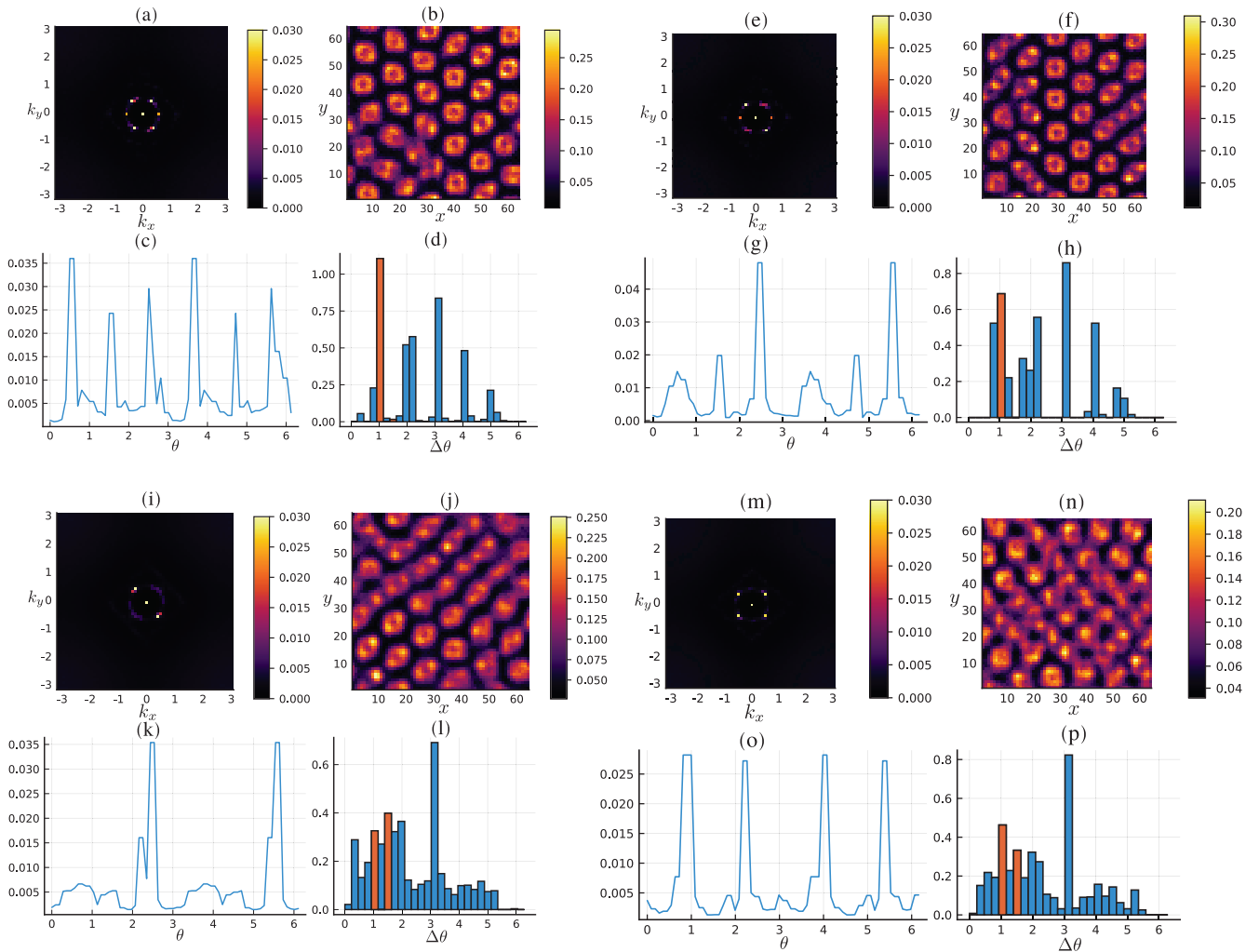

FIG. 11. A tableau of simulation results for the temperatures $T = \{1.7, 1.725, 1.742, 1.751\}$ in ascending order from left to right and top to bottom. The system has parameters $\nu = 0.1$, $g = 0.3$, and $f = 1/64$. The real space z-averaged vorticity in (b), (f), (j), and (n) exhibits both single and double quanta lattice structures. The remaining figures show the transition from signals of a hexagonal lattice to a square lattice as the temperature increases.
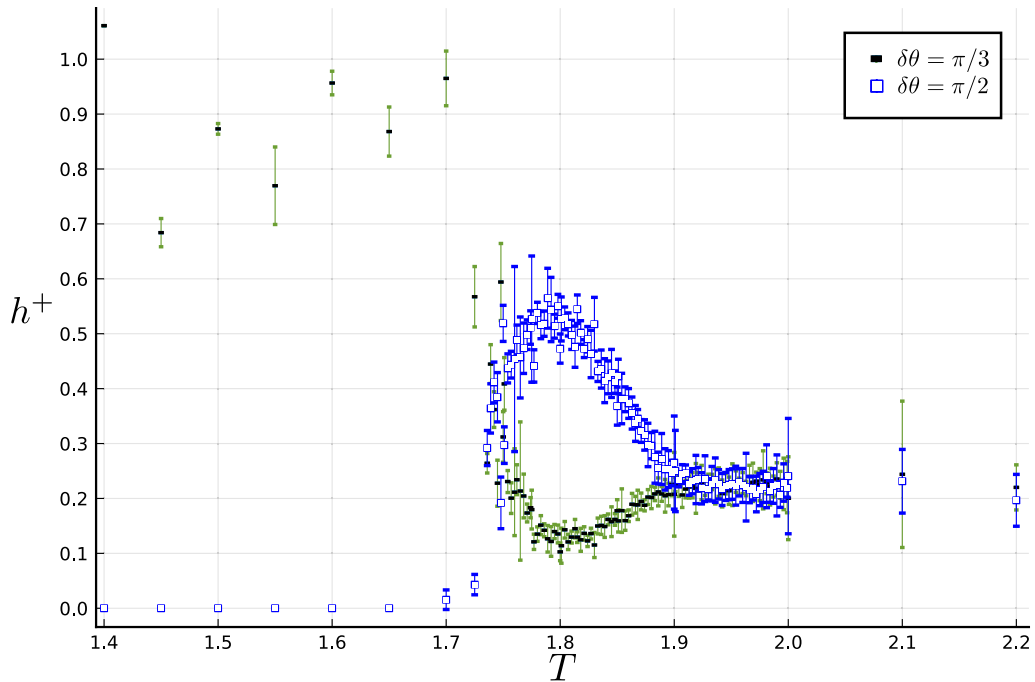
FIG. 12. Histogram temperature dependence for two different bins in a system with $f = 1/64$, $g = 0.3$, $\nu = 0.1$, and $L = 64$. The histogram is given by Eq. (32) and gives normalized bins of the angular distance $\Delta\theta$ between peaks in the structure function. The bin at $\Delta\theta = \pi/2$ corresponds to the signal of a square lattice structure in the structure function and is marked with blue hollow squares. The bin at $\Delta\theta = \pi/3$ is the signal for a hexagonal vortex lattice and is marked with black bar markers and green error bars. The transition from a doubly-quantized hexagonal lattice to a singly-quantized square lattice as T increases occurs at $T \approx 1.75$.

vortex lattice transitions, over a narrow temperature regime, to a square vortex lattice of singly-quantized vortices. At even higher temperatures, the vortex lattice structure function is washed out by thermally induced vortex loops when temperatures approach and cross the crossover line at $f = 1/64$, $T^* = 1.86 \pm 0.04$, rendering the system in a vortex-plasma phase. Our results indicate that double-quanta vortices can be quite robust and do not very easily dissociate into single quanta vortices when thermal fluctuations are included.

Thus, previous results, based on ground state computations and minimization of internal energy, predicting doubly-quantized hexagonal vortex lattices at low magnetic fields transitioning to singly-quantized square vortex lattices at higher magnetic fields very close to H_{c2}, are stable to fully accounting for entropic effects in the free energy. Therefore, double-quanta vortices are a quite robust property of chiral p-wave superconductors. Our results, however, do indicate a slight broadening of the temperature regime above which a square vortex lattice is entropically stabilized compared to earlier mean-field results. The main finding is that, for the regimes considered in the paper, this entropic stabilization does not significantly diminish the temperature range where a doubly-quantized hexagonal vortex state exists.
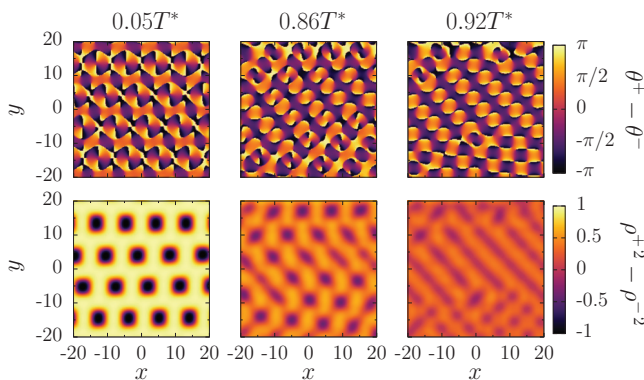
FIG. 13. Vortex phases of the mean-field theory in an external field for $g = 0.3$ and $\nu = 0.3$ with the corresponding filling fraction is $f_{\mathrm{MF}} \approx 1/30$. The panels on the top line display the relative phase Eq. (30) while the bottom line shows the relative densities defined in Eq. (35). Note that both relative phase and densities in the mean field are not thermal average.

APPENDIX A: DERIVATION OF EQ. (22)

Writing $\tan\theta^{\pm}$ in terms of the complex fields yields

$$\tan\theta^{\pm} = -i\frac{\eta^{\pm} - \eta^{\pm *}}{\eta^{\pm} + \eta^{\pm *}}. \tag{A1}$$

Inserting the transformation to the xy basis in Eq. (3) and making the London-limit approximation $|\eta^x| = |\eta^y|$, Eq. (A1) becomes

$$\tan\theta^h = \frac{\sin\theta^x + h\cos\theta^y}{\cos\theta^x - h\sin\theta^y}. \tag{A2}$$

Using the trigonometric identity

$$\sin x + \cos y = 2\sin\left(\frac{x-y}{2} + \frac{\pi}{4}\right)\sin\left(\frac{x+y}{2} + \frac{\pi}{4}\right), \tag{A3}$$

after including h and $-h$ in the argument of sin in the numerator and denominator of Eq. (A2) respectively, $\tan\theta^h$ can be written

$$\begin{aligned}
\tan\theta^h &= h\frac{\sin\left(\frac{h\theta^x - \theta^y}{2} + \frac{\pi}{4}\right)\sin\left(\frac{h\theta^x + \theta^y}{2} + \frac{\pi}{4}\right)}{\sin\left(-\frac{\theta^x + h\theta^y}{2} + \frac{\pi}{4}\right)\sin\left(\frac{\theta^x - h\theta^y}{2} + \frac{\pi}{4}\right)} \\
&= -h\frac{\sin\left(\frac{\theta^x + \theta^y}{2} + h\frac{\pi}{4}\right)}{\sin\left(\frac{\theta^x + \theta^y}{2} - h\frac{\theta}{4}\right)} \\
&= -\frac{1}{-\bar{h}\frac{\sin\left(\frac{\theta^x + \theta^y}{2} + \bar{h}\frac{\pi}{4}\right)}{\sin\left(\frac{\theta^x + \theta^y}{2} - \bar{h}\frac{\pi}{4}\right)}} = -\frac{1}{\tan\theta^{\bar{h}}}. \tag{A4}
\end{aligned}$$

This equation shows that both $\tan\theta^+$ and $\tan\theta^-$ are determined by one variable, $\theta^x + \theta^y$, which is what makes it possible to relate θ^+ to θ^-. Finally, by shifting the argument of the last tan we get Eq. (22), i.e., the relationship $\tan\theta^h = \tan(\theta^{\bar{h}} + \pi/2)$.

APPENDIX B: SYMMETRIZED MIXED GRADIENT TERM

Using the transformation properties of $\eta_{\mathbf{r}}^a$ and $A_{\mathbf{r},\mu}$ in Eqs. (24) and (25) on the expression for the discretized mixed gradient term in the xy basis in Eq. (19) repeated here for convenience:

$$\begin{aligned}
\mathcal{F}_{\mathrm{MG}}^{\mathrm{r}} = (1-\nu)\sum_a\Big[&\rho_{\mathbf{r}+\hat{x}}^a\rho_{\mathbf{r}+\hat{y}}^{\bar{a}}\cos\left(\theta_{\mathbf{r}+\hat{x}}^a - \theta_{\mathbf{r}+\hat{y}}^{\bar{a}} - (A_{\mathbf{r},x} - A_{\mathbf{r},y})\right) - \rho_{\mathbf{r}+\hat{x}}^a\rho_{\mathbf{r}}^{\bar{a}}\cos\left(\theta_{\mathbf{r}+\hat{x}}^a - \theta_{\mathbf{r}}^{\bar{a}} - A_{\mathbf{r},x}\right) \\
&- \rho_{\mathbf{r}+\hat{y}}^a\rho_{\mathbf{r}}^{\bar{a}}\cos\left(\theta_{\mathbf{r}+\hat{y}}^a - \theta_{\mathbf{r}}^{\bar{a}} - A_{\mathbf{r},y}\right) + \rho_{\mathbf{r}}^a\rho_{\mathbf{r}}^{\bar{a}}\cos\left(\theta_{\mathbf{r}}^a - \theta_{\mathbf{r}}^{\bar{a}}\right)\Big], \tag{B1}
\end{aligned}$$

we obtain the rotated mixed gradient terms

$$\begin{aligned}
C_4\mathcal{F}_{\mathrm{MG}}^{\mathrm{r}} = -(1-\nu)\sum_a\Big[&\rho_{\mathbf{r}-\hat{x}}^a\rho_{\mathbf{r}+\hat{y}}^{\bar{a}}\cos\left(\theta_{\mathbf{r}-\hat{x}}^a - \theta_{\mathbf{r}+\hat{y}}^{\bar{a}} + (A_{\mathbf{r},y} + A_{\mathbf{r}-\hat{x},x})\right) - \rho_{\mathbf{r}-\hat{x}}^a\rho_{\mathbf{r}}^{\bar{a}}\cos\left(\theta_{\mathbf{r}-\hat{x}}^a - \theta_{\mathbf{r}}^{\bar{a}} + A_{\mathbf{r}-\hat{x},x}\right) \\
&- \rho_{\mathbf{r}}^a\rho_{\mathbf{r}+\hat{y}}^{\bar{a}}\cos\left(\theta_{\mathbf{r}}^a - \theta_{\mathbf{r}+\hat{y}}^{\bar{a}} + A_{\mathbf{r},y}\right) + \rho_{\mathbf{r}}^a\rho_{\mathbf{r}}^{\bar{a}}\cos\left(\theta_{\mathbf{r}}^a - \theta_{\mathbf{r}}^{\bar{a}}\right)\Big], \tag{B2}
\end{aligned}$$

$$\begin{aligned}
C_4^2\mathcal{F}_{\mathrm{MG}}^{\mathrm{r}} = (1-\nu)\sum_a\Big[&\rho_{\mathbf{r}-\hat{x}}^a\rho_{\mathbf{r}-\hat{y}}^{\bar{a}}\cos\left(\theta_{\mathbf{r}-\hat{x}}^a - \theta_{\mathbf{r}-\hat{y}}^{\bar{a}} - (A_{\mathbf{r}-\hat{y},y} - A_{\mathbf{r}-\hat{x},x})\right) - \rho_{\mathbf{r}-\hat{x}}^a\rho_{\mathbf{r}}^{\bar{a}}\cos\left(\theta_{\mathbf{r}-\hat{x}}^a - \theta_{\mathbf{r}}^{\bar{a}} + A_{\mathbf{r}-\hat{x},x}\right) \\
&- \rho_{\mathbf{r}}^a\rho_{\mathbf{r}-\hat{y}}^{\bar{a}}\cos\left(\theta_{\mathbf{r}-\hat{y}}^{\bar{a}} - \theta_{\mathbf{r}}^a + A_{\mathbf{r}-\hat{y},y}\right) + \rho_{\mathbf{r}}^a\rho_{\mathbf{r}}^{\bar{a}}\cos\left(\theta_{\mathbf{r}}^a - \theta_{\mathbf{r}}^{\bar{a}}\right)\Big], \tag{B3}
\end{aligned}$$

$$\begin{aligned}
C_4^3\mathcal{F}_{\mathrm{MG}}^{\mathrm{r}} = -(1-\nu)\sum_a\Big[&\rho_{\mathbf{r}-\hat{y}}^{\bar{a}}\rho_{\mathbf{r}+\hat{x}}^a\cos\left(\theta_{\mathbf{r}-\hat{y}}^{\bar{a}} - \theta_{\mathbf{r}+\hat{x}}^a + (A_{\mathbf{r}-\hat{y},y} + A_{\mathbf{r},x})\right) - \rho_{\mathbf{r}-\hat{y}}^{\bar{a}}\rho_{\mathbf{r}}^a\cos\left(\theta_{\mathbf{r}-\hat{y}}^{\bar{a}} - \theta_{\mathbf{r}}^a + A_{\mathbf{r}-\hat{y},y}\right) \\
&- \rho_{\mathbf{r}}^{\bar{a}}\rho_{\mathbf{r}+\hat{x}}^a\cos\left(\theta_{\mathbf{r}+\hat{x}}^a - \theta_{\mathbf{r}}^{\bar{a}} - A_{\mathbf{r},x}\right) + \rho_{\mathbf{r}}^{\bar{a}}\rho_{\mathbf{r}}^a\cos\left(\theta_{\mathbf{r}}^{\bar{a}} - \theta_{\mathbf{r}}^a\right)\Big]. \tag{B4}
\end{aligned}$$

In these expressions, $a, q \in \{x, y\}$. Adding Eqs. (B1)–(B4), several terms cancel. As is immediately obvious, all the onsite terms such as the last term in Eq. (B1) cancel each other. Considering the last term on the first line of Eq. (B2), we let $\mathbf{r} \to \mathbf{r} + \hat{x}$ which is allowed because of periodic boundary conditions, and we see that this cancels the last term on the first line of Eq. (B1). The first term on the last line of Eqs. (B2) and (B1) can be seen to cancel through a simple relabeling of the a summation index. The same cancellations happen for the analogous terms in Eqs. (B3) and (B4) such that the average of Eqs. (B1)–(B4) and thus the full symmetrized expression for the mixed gradient terms can be written on the simple form

$$\mathcal{F}_{\mathrm{MG}}^{\mathrm{s}} = \frac{(1-\nu)}{4}\sum_a\sum_{h,h'=\pm} hh'\rho_{\mathbf{r}+h\hat{x}}^a\rho_{\mathbf{r}+h'\hat{y}}^{\bar{a}}\cos\left(\theta_{\mathbf{r}+h\hat{x}}^a - \theta_{\mathbf{r}+h'\hat{y}}^{\bar{a}} - A_{\mathbf{r},hx} + A_{\mathbf{r},h'y}\right). \tag{B5}$$

This expression, together with Eqs. (15), (16), (17), and (18), constitute the free energy used in the simulations.

APPENDIX C: NUMERICAL BASIS ROTATION

In this Appendix, we present the numerical details for how chiral matter field amplitudes and phases are calculated from their xy-basis counterparts. The chiral amplitudes $\rho_{\mathbf{r}}^h$ are easily found from the xy-basis variables through Eq. (20):

$$\rho_{\mathbf{r}}^h = \sqrt{\frac{\rho^{x\,2} + \rho^{y\,2}}{2} + h\rho^x\rho^y \sin\left(\theta_{\mathbf{r}}^x - \theta_{\mathbf{r}}^y\right)}. \quad \text{(C1)}$$

The chiral phases are obtained by the set of equations

$$\sin\theta_{\mathbf{r}}^h = \frac{\rho^x \sin\theta_{\mathbf{r}}^x + h\rho^y \cos\theta_{\mathbf{r}}^y}{\sqrt{2}\rho_{\mathbf{r}}^h}, \quad \text{(C2)}$$

$$\cos\theta_{\mathbf{r}}^h = \frac{\rho^x \cos\theta_{\mathbf{r}}^x - h\rho^y \sin\theta_{\mathbf{r}}^y}{\sqrt{2}\rho_{\mathbf{r}}^h}. \quad \text{(C3)}$$

As long as $\rho_{\mathbf{r}}^h > 0$, $\theta_{\mathbf{r}}^h \in [-\pi, \pi)$ can be found through simple trigonometric relations which we include for completeness. Given that $\cos\theta_{\mathbf{r}}^h > 0$ then $\theta_{\mathbf{r}}^h = \tan^{-1}\tan\theta_{\mathbf{r}}^h$. If $\cos\theta_{\mathbf{r}}^h < 0$ then $\theta_{\mathbf{r}}^h = \tan^{-1}\tan\theta_{\mathbf{r}}^h - \pi\,\mathrm{sgn}\tan\theta_{\mathbf{r}}^h$. The final case is that $\cos\theta_{\mathbf{r}}^h = 0$ in which case $\theta_{\mathbf{r}}^h = \pi/2\,\mathrm{sgn}\sin\theta_{\mathbf{r}}^h$.

In the chiral ground state of the system $\theta_{\mathbf{r}}^x - \theta_{\mathbf{r}}^y \to -h\pi/2$ which makes $\rho_{\mathbf{r}}^h \to 0$ when $\rho^x = \rho^y$. This makes Eqs. (C2) and (C3) numerically unstable as both numerator and de-

nominator approach zero. To accurately calculate $\theta_{\mathbf{r}}^h$, these equations are expanded around the ground state value. Setting $\theta_{\mathbf{r}}^x - \theta_{\mathbf{r}}^y = -h\pi/2 + 2\pi n + \delta$ and expanding to fourth order in δ yields

$$\sin\theta_{\mathbf{r}}^h \to \frac{\delta}{|\delta|}\cos\theta_{\mathbf{r}}^x\left[1 - \frac{\delta^2}{8} + \frac{\delta^4}{384}\right]$$
$$- \frac{|\delta|}{2}\sin\theta_{\mathbf{r}}^x\left[1 - \frac{\delta^2}{24} + \frac{\delta^4}{1920}\right], \quad \text{(C4a)}$$

$$\cos\theta_{\mathbf{r}}^h \to \frac{|\delta|}{2}\cos\theta_{\mathbf{r}}^x\left[1 - \frac{\delta^2}{24} + \frac{\delta^4}{1920}\right]$$
$$- \frac{\delta}{|\delta|}\sin\theta_{\mathbf{r}}^x\left[1 - \frac{\delta^2}{8} + \frac{\delta^4}{384}\right]. \quad \text{(C4b)}$$

The expressions on the right are independent of h. Then if $\sin\theta_{\mathbf{r}}^h \leqslant 0$, $\theta_{\mathbf{r}}^h = -\cos^{-1}\cos\theta_{\mathbf{r}}^h$. If not, then $\theta_{\mathbf{r}}^h = \cos^{-1}\cos\theta_{\mathbf{r}}^h$. To find δ we simply calculate $\delta = \mod(\theta_{\mathbf{r}}^x - \theta_{\mathbf{r}}^y, 2\pi) - 3\pi/2$ for $h = +$ and $\delta = \mod(\theta_{\mathbf{r}}^x - \theta_{\mathbf{r}}^y, 2\pi) - \pi/2$ for $h = -$. With this expansion in δ, the errors from calculating $\theta_{\mathbf{r}}^h$ were found to be smaller than the floating point error.

[1] D. D. Osheroff, W. J. Gully, R. C. Richardson, and D. M. Lee, New Magnetic Phenomena in Liquid He^3 Below 3 mK, Phys. Rev. Lett. **29**, 920 (1972).

[2] D. D. Osheroff, R. C. Richardson, and D. M. Lee, Evidence for a New Phase of Solid He^3, Phys. Rev. Lett. **28**, 885 (1972).

[3] A. Leggett, The spin dynamics of an anisotropic fermi superfluid (^{3}He?), Ann. Phys. **85**, 11 (1974).

[4] A. J. Leggett, A theoretical description of the new phases of liquid ^{3}He, Rev. Mod. Phys. **47**, 331 (1975).

[5] Note that we deliberately avoid the use of the term order parameter when discussing the matter field. The reason is, while the identification of the matter field as a local order parameter would be perfectly fine in a $3D$ superfluid, this is not so for a superconductor. In a superconductor, with a charged condensate coupling minimally to a gauge field, there exists no local order parameter in any dimension, at any temperature [68]. Throughout our paper, we simply refer to what is normally called the superconducting order parameter as a *field*. Under certain circumstances the Higgs mass of the gauge field acquired upon entering the superconducting state may be interpreted as an order parameter.

[6] N. D. Mermin and T.-L. Ho, Circulation and Angular Momentum in the *A* Phase of Superfluid Helium-3, Phys. Rev. Lett. **36**, 594 (1976).

[7] P. W. Anderson and G. Toulouse, Phase Slippage without Vortex Cores: Vortex Textures in Superfluid ^{3}He, Phys. Rev. Lett. **38**, 508 (1977).

[8] N. D. Mermin, The topological theory of defects in ordered media, Rev. Mod. Phys. **51**, 591 (1979).

[9] Y. Maeno, H. Hashimoto, K. Yoshida, S. Nishizaki, T. Fujita, J. G. Bednorz, and F. Lichtenberg, Superconductivity in a layered perovskite without copper, Nature (London) **372**, 532 (1994).

[10] A. P. Mackenzie, S. R. Julian, A. J. Diver, G. J. McMullan, M. P. Ray, G. G. Lonzarich, Y. Maeno, S. Nishizaki, and T. Fujita, Quantum Oscillations in the Layered Perovskite Superconductor Sr$_2$RuO$_4$, Phys. Rev. Lett. **76**, 3786 (1996).

[11] Y. Maeno, M. Rice, and M. Sigrst, The intriguing superconductivity of Sr$_2$RuO$_4$, Phys. Today **54**(1), 42 (2001).

[12] A. P. Mackenzie, T. Scaffidi, C. W. Hicks, and Y. Maeno, Even odder after twenty-three years: the superconducting order parameter puzzle of Sr$_2$RuO$_4$, npj Quantum Mater. **2**, 40 (2017).

[13] A. P. Mackenzie, R. K. W. Haselwimmer, A. W. Tyler, G. G. Lonzarich, Y. Mori, S. Nishizaki, and Y. Maeno, Extremely Strong Dependence of Superconductivity on Disorder in Sr$_2$RuO$_4$, Phys. Rev. Lett. **80**, 161 (1998).

[14] A. P. Mackenzie and Y. Maeno, The superconductivity of Sr$_2$RuO$_4$ and the physics of spin-triplet pairing, Rev. Mod. Phys. **75**, 657 (2003).

[15] K. Ishida, H. Mukuda, Y. Kitaoka, K. Asayama, Z. Q. Mao, Y. Mori, and Y. Maeno, Spin-triplet superconductivity in Sr$_2$RuO$_4$ identified by ^{17}O Knight shift, Nature (London) **396**, 658 (1998).

[16] K. Ishida, M. Manago, T. Yamanaka, H. Fukazawa, Z. Q. Mao, Y. Maeno, and K. Miyake, Spin polarization enhanced by spin-triplet pairing in Sr$_2$RuO$_4$ probed by NMR, Phys. Rev. B **92**, 100502(R) (2015).

[17] K. Izawa, H. Takahashi, H. Yamaguchi, Y. Matsuda, M. Suzuki, T. Sasaki, T. Fukase, Y. Yoshida, R. Settai, and Y. Onuki, Superconducting Gap Structure of Spin-Triplet Superconductor Sr$_2$RuO$_4$ Studied by Thermal Conductivity, Phys. Rev. Lett. **86**, 2653 (2001).

[18] S. Nishizaki, Y. Maeno, S. Farner, S.-i. Ikeda, and T. Fujita, Evidence for unconventional superconductivity of Sr$_2$RuO$_4$ from specific-heat measurements, J. Phys. Soc. Jpn. **67**, 560 (1998).

[19] I. A. Firmo, S. Lederer, C. Lupien, A. P. Mackenzie, J. C. Davis, and S. A. Kivelson, Evidence from tunneling spectroscopy for a quasi-one-dimensional origin of superconductivity in Sr_2RuO_4, Phys. Rev. B **88**, 134521 (2013).

[20] G. M. Luke, Y. Fudamoto, K. M. Kojima, M. I. Larkin, J. Merrin, B. Nachumi, Y. J. Uemura, Y. Maeno, Z. Q. Mao, Y. Mori, H. Nakamura, and M. Sigrist, Time-reversal symmetry-breaking superconductivity in Sr_2RuO_4, Nature (London) **394**, 558 (1998).

[21] J. Xia, Y. Maeno, P. T. Beyersdorf, M. M. Fejer, and A. Kapitulnik, High Resolution Polar Kerr Effect Measurements of Sr_2RuO_4: Evidence for Broken Time-Reversal Symmetry in the Superconducting State, Phys. Rev. Lett. **97**, 167002 (2006).

[22] V. Grinenko, S. Ghosh, R. Sarkar, J.-C. Orain, A. Nikitin, M. Elender, D. Das, Z. Guguchia, F. Br uckner, M. E. Barber, J. Park, N. Kikugawa, D. A. Sokolov, J. S. Bobowski, T. Miyoshi, Y. Maeno, A. P. Mackenzie, H. Luetkens, C. W.Hicks, and H.-H. Klauss, Split superconducting and time-reversal symmetry-breaking transitions, and magnetic order in Sr_2RuO_4 under uniaxial stress, Nat. Phys. **17**, 748 (2021).

[23] P. J. Curran, S. J. Bending, W. M. Desoky, A. S. Gibbs, S. L. Lee, and A. P. Mackenzie, Search for spontaneous edge currents and vortex imaging in Sr_2RuO_4 mesostructures, Phys. Rev. B **89**, 144504 (2014).

[24] A. Pustogow, Y. Luo, A. Chronister, Y.-S. Su, D. A. Sokolov, F. Jerzembeck, A. P. Mackenzie, C. W. Hicks, N. Kikugawa, S. Raghu, E. D. Bauer, and S. E. Brown, Constraints on the superconducting order parameter in Sr_2RuO_4 from oxygen-17 nuclear magnetic resonance, Nature (London) **574**, 72 (2019).

[25] S. Benhabib, C. Lupien, I. Paul, L. Berges, M. Dion, M. Nardone, A. Zitouni, Z. Mao, Y. Maeno, A. Georges *et al.*, Ultrasound evidence for a two-component superconducting order parameter in Sr_2RuO_4, Nat. Phys. **17**, 194 (2021).

[26] S. Ghosh, A. Shekhter, F. Jerzembeck, N. Kikugawa, D. A. Sokolov, M. Brando, A. Mackenzie, C. W. Hicks, and B. Ramshaw, Thermodynamic evidence for a two-component superconducting order parameter in Sr_2RuO_4, Nat. Phys. **17**, 199 (2021).

[27] S. J. Ray, A. S. Gibbs, S. J. Bending, P. J. Curran, E. Babaev, C. Baines, A. P. Mackenzie, and S. L. Lee, Muon-spin rotation measurements of the vortex state in Sr_2RuO_4: Type-1.5 superconductivity, vortex clustering, and a crossover from a triangular to a square vortex lattice, Phys. Rev. B **89**, 094504 (2014).

[28] S. A. Kivelson, A. C. Yuan, B. J. Ramshaw, and R. Thomale, A proposal for reconciling diverse experiments on the superconducting state in Sr_2RuO_4, npj Quantum Mater. **5**, 43 (2020).

[29] A. T. Rømer, D. D. Scherer, I. M. Eremin, P. J. Hirschfeld, and B. M. Andersen, Knight Shift and Leading Superconducting Instability from Spin Fluctuations in Sr_2RuO_4, Phys. Rev. Lett. **123**, 247001 (2019).

[30] T. A. Tokuyasu, D. W. Hess, and J. A. Sauls, Vortex states in an unconventional superconductor and the mixed phases of UPt_3, Phys. Rev. B **41**, 8891 (1990).

[31] K. E. Avers, W. J. Gannon, S. J. Kuhn, W. P. Halperin, J. A. Sauls, L. DeBeer-Schmitt, C. D. Dewhurst, J. Gavilano, G. Nagy, U. Gasser, and M. R. Eskildsen, Broken time-reversal symmetry in the topological superconductor UPt_3, Nat. Phys. **16**, 531 (2020).

[32] T. Tokuyasu and J. Sauls, Stability of doubly quantized vortices in unconventional superconductors, Physica B+C **165-166**, 347 (1990).

[33] M. Sigrist and K. Ueda, Phenomenological theory of unconventional superconductivity, Rev. Mod. Phys. **63**, 239 (1991).

[34] D. F. Agterberg, Vortex Lattice Structures of Sr_2RuO_4, Phys. Rev. Lett. **80**, 5184 (1998).

[35] R. Heeb and D. F. Agterberg, Ginzburg-Landau theory for a p-wave Sr_2RuO_4 superconductor: Vortex core structure and extended London theory, Phys. Rev. B **59**, 7076 (1999).

[36] J. Garaud and E. Babaev, Properties of skyrmions and multiquanta vortices in chiral p-wave superconductors, Sci. Rep. **5**, 17540 (2015).

[37] J. Garaud and E. Babaev, Skyrmionic state and stable half-quantum vortices in chiral p-wave superconductors, Phys. Rev. B **86**, 060514(R) (2012).

[38] J. A. Sauls and M. Eschrig, Vortices in chiral, spin-triplet superconductors and superfluids, New J. Phys. **11**, 075008 (2009).

[39] J. Garaud, E. Babaev, T. A. Bojesen, and A. Sudbø, Lattices of double-quanta vortices and chirality inversion in $p_x + ip_y$ superconductors, Phys. Rev. B **94**, 104509 (2016).

[40] S. B. Chung and S. A. Kivelson, Entropy-driven formation of a half-quantum vortex lattice, Phys. Rev. B **82**, 214512 (2010).

[41] C. Dasgupta and B. I. Halperin, Phase Transition in a Lattice Model of Superconductivity, Phys. Rev. Lett. **47**, 1556 (1981).

[42] M. E. Peskin, Mandelstam-'t Hooft duality in abelian lattice models, Ann. Phys. (NY) **113**, 122 (1978).

[43] H. Kleinert, *Gauge Fields in Condensed Matter: Vol. 1: Superflow and Vortex Lines (Disorder Fields, Phase Transitions) Vol. 2: Stresses and Defects (Differential Geometry, Crystal Melting)* (World Scientific, Singapore, 1989).

[44] S. Mo, J. Hove, and A. Sudbø, Order of the metal-to-superconductor transition, Phys. Rev. B **65**, 104501 (2002).

[45] J. Smiseth, E. Smørgrav, E. Babaev, and A. Sudbø, Field- and temperature-induced topological phase transitions in the three-dimensional N-component london superconductor, Phys. Rev. B **71**, 214509 (2005).

[46] K. Fossheim and A. Sudbø, *Superconductivity: Physics and Applications* (John Wiley & Sons, Chichester, 2005).

[47] M. Speight, T. Winyard, and E. Babaev, Chiral p-wave superconductors have complex coherence and magnetic field penetration lengths, Phys. Rev. B **100**, 174514 (2019).

[48] F. N. Krohg and A. Sudbø, Derivation of a Ginzburg-Landau free energy density of a $p + ip$ superconductor from spin-orbit coupling with mixed gradient terms, Phys. Rev. B **98**, 014510 (2018).

[49] D. F. Agterberg, Square vortex lattices for two-component superconducting order parameters, Phys. Rev. B **58**, 14484 (1998).

[50] J.-X. Zhu, C. S. Ting, J. L. Shen, and Z. D. Wang, Ginzburg-Landau equations for layered p-wave superconductors, Phys. Rev. B **56**, 14093 (1997).

[51] G. Münster and M. Walzl, Lattice gauge theory - a short primer, arXiv:hep-lat/0012005.

[52] P. N. Galteland, E. Babaev, and A. Sudbø, Fluctuation effects in rotating Bose-Einstein condensates with broken $SU(2)$ and $U(1) \times U(1)$ symmetries in the presence of intercomponent density-density interactions, Phys. Rev. A **91**, 013605 (2015).

[53] A. Shimizu, H. Ozawa, I. Ichinose, and T. Matsui, Lattice Ginzburg-Landau model of a ferromagnetic *p*-wave pairing phase in superconducting materials and an inhomogeneous co-existing state, Phys. Rev. B **85**, 144524 (2012).

[54] A. K. Nguyen and A. Sudbø, Topological phase fluctuations, amplitude fluctuations, and criticality in extreme type-II super-conductors, Phys. Rev. B **60**, 15307 (1999).

[55] A. K. Nguyen and A. Sudbø, A new broken $U(1)$-symmetry in extreme type-II superconductors, Europhys. Lett. **46**, 780 (1999).

[56] W. K. Hastings, Monte carlo sampling methods using markov chains and their applications, Biometrika **57**, 97 (1970).

[57] H. G. Katzgraber, Introduction to Monte Carlo methods, arXiv:0905.1629.

[58] W. H. Press, S. A. Teukolsky, W. T. Vetterlig, and B. P. Flannery, *Numerical Recipes*, 3rd ed. (Cambridge University Press, New York, 2007).

[59] M. Newman and G. Barkema, *Monte Carlo Methods in Statistical Physics* (Clarendon Press, Oxford, 1999).

[60] J. Bezanson, A. Edelman, S. Karpinski, and V. B. Shah, Julia: A fresh approach to numerical computing, SIAM Rev. **59**, 65 (2017).

[61] M. Matsumoto and T. Nishimura, Mersenne twister: A 623-dimensionally equidistributed uniform pseudo-random number generator, ACM Trans. Model. Comput. Simul. **8**, 3 (1998).

[62] Y.-H. Li and S. Teitel, Vortex-line fluctuations in model high-temperature superconductors, Phys. Rev. B **47**, 359 (1993).

[63] S. Kragset, E. Babaev, and A. Sudbø, Effects of boundaries and density inhomogeneity on states of vortex matter in Bose-Einstein condensates at finite temperature, Phys. Rev. A **77**, 043605 (2008).

[64] A. M. Ferrenberg and R. H. Swendsen, New Monte Carlo Technique for Studying Phase Transitions, Phys. Rev. Lett. **61**, 2635 (1988).

[65] A. M. Ferrenberg and R. H. Swendsen, Optimized Monte Carlo Data Analysis, Phys. Rev. Lett. **63**, 1195 (1989).

[66] J. Nocedal and S. J. Wright, Trust-region methods, in *Numerical Optimization* (Springer, New York, 2006), Chap. 4, pp. 66–100.

[67] B. Efron, Bootstrap methods: Another look at the jackknife, The Annals of Statistics **7**, 1 (1979).

[68] S. Elitzur, Impossibility of spontaneously breaking local symmetries, Phys. Rev. D **12**, 3978 (1975).